DYNAMIC PRESSURE IMPROVEMENTS TO CLOSED-CIRCUIT WIND TUNNELS WITH FLOW QUALITY ANALYSIS

A Thesis

by

ALEXANDER KELLY HERRING

Submitted to the Office of Graduate and Professional Studies of
Texas A&M University
in partial fulfillment of the requirements for the degree of

MASTER OF SCIENCE

Chair of Committee,	Edward White
Committee Member,	Orthon K. Rediniotis
	Yong-Joe Kim
Head of Department,	Rodney Bowersox

May 2015

Major Subject: Aerospace Engineering

ABSTRACT

Testing of aerodynamic loads on a sub-scale model has been the most accurate way to predict full-scale loads for many years. Even with modern advances in computing technology and computational fluid dynamics (CFD), each computer-aided model must be calibrated against a known standard, usually found through wind tunnel testing. Because wind tunnel testing is usually performed on sub-scale models, flow speeds that span the flight envelope are commonly tested. Traditionally the Texas A&M Engineering Experiment Station Low-Speed Wind Tunnel (LSWT) was limited through available power to a dynamic pressure of 120 psf. The addition of a higher power motor, construction of a new, smaller test section, diffuser liners to prevent flow separation, and increased structure to withstand higher static pressures allows for flow speeds up to 240 psf, nominally Mach 0.4. With proper design and construction, flow quality can be maintained to less than 1% deviation from mean flow velocity. Additionally, an accurate prediction of flow speed for a given test section geometry and power draw can be found.

ACKNOWLEDGEMENTS

I would like to first thank my advisor, Dr. Ed White. His guidance and reassurance during this long process have made this thesis possible. Thank you to my committee members, Dr. Orthon Rediniotis, and Dr. Yong-Joe Kim for their assistance with this work. The staff of the Oran W. Nicks Low Speed Wind Tunnel have provided unwaivering support of these goals. In particular I would like to thank my colleagues Doug Kutz, Lisa Brown, Ric Warren, and John Kochan for their moral and technical support during the seemingly endless hours of installation and fine-tuning of this test. I would also like to thank my family and friends for their understanding and encouragement, even through the difficult times.

TABLE OF CONTENTS

LIST OF FIGURES

LIST OF TABLES

1. INTRODUCTION

1.1 Background and Objective

Wind tunnel testing has remained one of the dominant techniques for measuring aerodynamic loads on a wide range of vehicles and structures. With computer technology constantly growing, aerodynamic performance simulation continues to improve. However, the Navier-Stokes equations which govern the characteristics of fluid flow can only be solved analytically for a few idealized cases. For the cases in which only a numerical solution exists, some complex phenomena are beyond the reach of modern computers. Wind tunnel testing allows for examination of these phenomena without the need of complex computer algorithms.

Wind tunnel testing is not without drawbacks, however. The cost associated with running a detailed analysis of flight characteristics can run extremely high, especially in the scope of an ever-changing aircraft design. For this reason wind tunnel testing is usually used as a means of verifying the results of a computer simulation on a small number of test configurations. It is important to span the entire flight envelope with testing to avoid excess extrapolation from the measured data.

Wind tunnels vary greatly depending on the testing envelope for which they were designed. The Texas A&M Engineering Experiment Station Low-Speed Wind Tunnel (LSWT) was designed and built in the mid 1940's as an open circuit wind tunnel. Shortly after performing an initial round of experiments the decision was made to enclose the circuit creating the LSWT configuration which remains to this day. Construction began on this closed circuit in 1958. Figure 1.1 shows this stage of construction.

Figure 1.1: LSWT closed-circuit construction c.1958 [1][2]

The decision to modify the current LSWT configuration was reached when inquiries into the ability to test up to and including Mach 0.4 were received. This speed is necessary to explore the behavior of retreating helicopter blades during dynamic stall. At this flow velocity a shock wave can form at the pressure minimum of the blade creating a violent stall behavior. Currently, the LSWT's 7 x 10 ft test section can achieve Mach 0.26. Both Guthery[1] and Sahoo[4] predicted that Mach 0.4 would be possible using a reduced test section size.

This thesis will examine predictions of flow speed for a reduced test section geometry, as well as outline the design and manufacture of a more efficient diffuser to correct for separation experienced by Sahoo. Finally, after the manufacture and installation of the diffuser, flow quality will be verified against the average flow velocity and the predictions outlined in Section 3 will be compared to actual test data.

1.2   Wind Tunnel Design Introduction

Subsonic wind tunnels are generally classified into one of two types, open circuit or closed circuit. Open circuit wind tunnels are characterized by the fluid flow traveling generally in a straight line. The flow travels through a contraction into the test section, and finally past the power section and is exhausted into the atmosphere. While the construction of an open circuit wind tunnel is typically less expensive, Barlow et al.[6] outlines several disadvantages including increased noise and reduced efficiency. Figure 1.2 shows the LSWT as originally constructed in an open circuit configuration. In contrast, closed circuit wind tunnels enclose the flow requiring little to no interaction with the environment. This increases efficiency, especially at higher speeds.
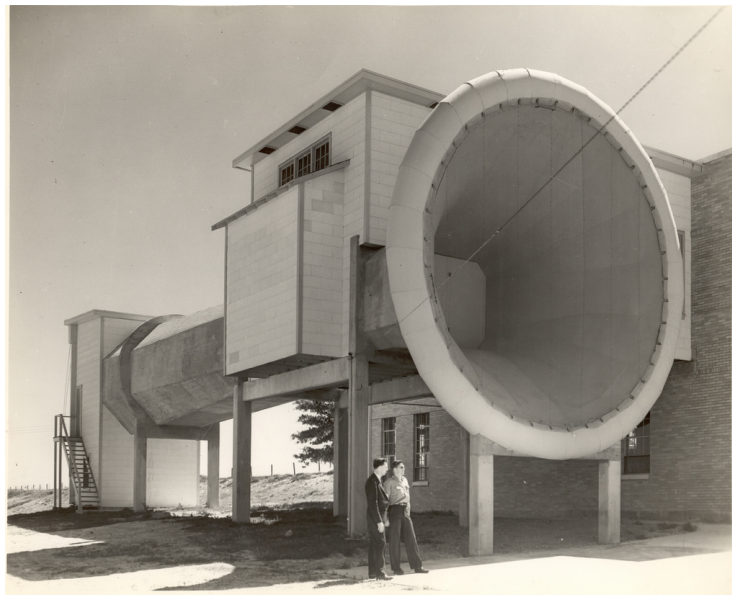
Figure 1.2: LSWT in original open circuit configuration c.1940's [1][3]

Wind tunnels are characterized by their test section size in addition to classification based on geometry. Flow similarity is the concept that, by nondimensionalizing the forces and moments, it is only important to match key parameters of a flow on a sub-scale model to describe the full scale results. The Reynolds number is given in Equation 1.1 and is the primary parameter which must be matched, where the subscript ∞ denotes free stream conditions, and l is a reverence length. Barlow et al. outlines best practices for determining this Reynolds number. This allows the design of wind tunnels which accommodate scale models rather than full scale vehicles. The LSWT as designed has a test section of 7 x 10 ft, this falls into the typical range for commercial wind tunnel testing.

$$R_{\mathrm{e}} = \frac{\rho_\infty V_\infty l}{\mu_\infty} \tag{1.1}$$

For a closed circuit wind tunnel, additional design considerations are required to maintain efficiency and uniformity. Efficiency can be reduced by both loss of pressure and friction. Guthery citing Barlow et al. outlines how each of portion of a wind tunnel can contribute to this overall loss. For closed circuit wind tunnels the fluid flow must be redirected around the circuit and back towards the start of the test section requiring multiple turns and an increased number of diffusers and ducts. In 2013 Guthery [1] performed a detailed analysis on the entire LSWT circuit. He found that the critical component for reducing the test section geometry while maintaining efficiency was the diffuser directly between the test section and power station of the LSWT.

2. LOW SPEED WIND TUNNEL FACILITY

Section 1 introduced the motivation to achieve wind tunnel testing speeds in the mid-subsonic range. This section will provide an overview of the the LSWT which serves a variety of industries by providing wind tunnel testing, and data analysis. The elements of the LSWT discussed in this section will be referenced in later sections to support design and testing decisions.

2.1 Facility Overview

The LSWT, as seen in Figure 2.1, is a closed circuit wind tunnel with a circuit length of 398 feet measured at the centerline. From the power section, just downstream of the diffuser, to the entrance of the contraction cone, the cross section is circular. The tunnel reaches its maximum diameter of 30 feet in the settling chamber, just upstream of the contraction. Turning vanes at each of the tunnel's four 90° turns help maintain flow quality. In addition to the turning vanes, two screens upstream of the contraction improve flow uniformity and reduced turbulence. The 30-ft-long contraction section transitions from circular cross section to the octagonal test section. The contraction ratio is 10.4.
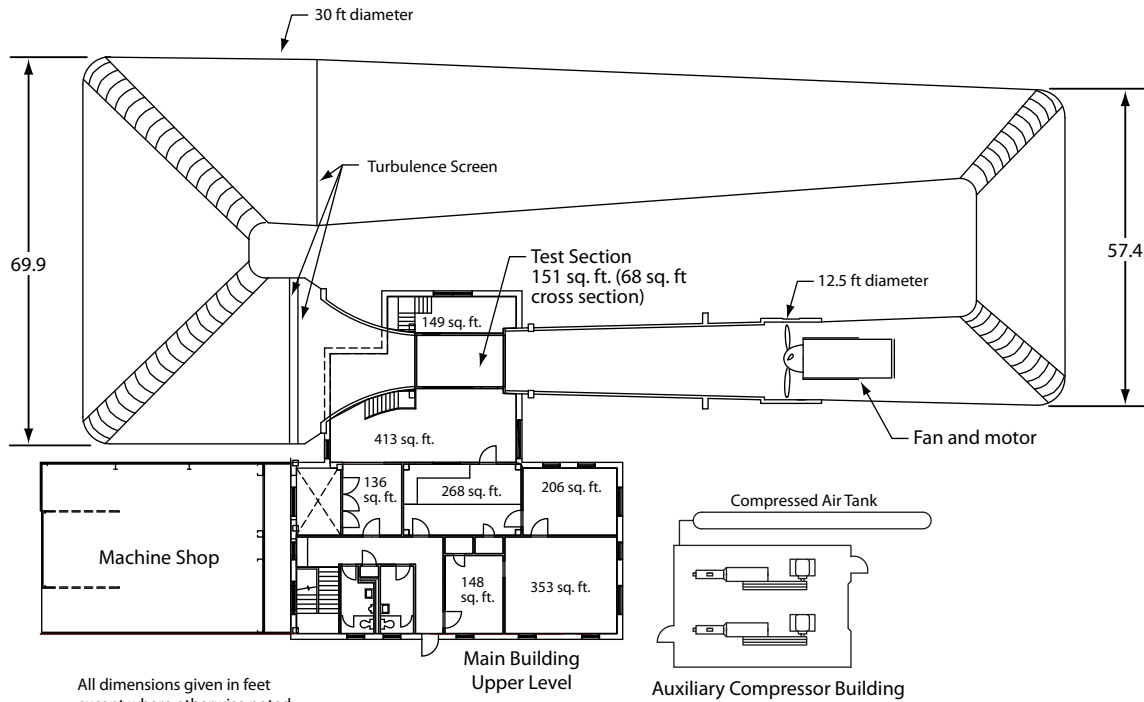
Figure 2.1: Schematic of the LSWT complex

The test section of the LSWT is 14-ft-long, with a cross section of 7 feet high and 10 feet across with one-foot 45° chamfers on each corner. The cross sectional area is 68 ft^2. In order to maintain test section static pressure near atmospheric levels, two three inch wide vertical venting slots are located in the side walls at the test section exit. Over the first 12 feet of the test section, the side walls diverge by 1 inch to account for boundary layer growth. Access to the test section is through a removable ceiling with an overhead hoist. Visual access to the model during testing is provided by large glass panels on the test section walls, and fluorescent lights positioned on the corner chamfers.

A 46-ft-long diffuser provides the transition from the octagonal test section to a circular cross section at the power section. The diffuser has expansion angles of 1.43° horizontally, and 3.83° vertically. The power section is comprised of a 3000 hp

TECO-Westinghouse electric motor and a 12.5-ft-diameter, four-blade Curtiss Electric propeller. The motor is equipped with a variable frequency drive system in order to vary the revolutions per minute (RPM) and the propeller is attached to a variable pitch system. With the variable pitch and rotation speed of the power station, test section dynamic pressures can range from zero to 120 psf.

The LSWT is equipped with a three-axis traversing mechanism (TM) which is used to mount hotwires and pressure probes. The TM can achieve automated motion in the plane normal to the flow direction, with the third component of motion being set manually. The TM system has a repeatable accuracy of 0.01 inches.

Models can be mounted in various ways, however most mount to a 7 foot diameter turntable which rests in the center of the test section floor and rotates with the external balance system. This turntable can be configured to allow access to the external balance or to mount struts for internal balance testing.

For internal balance tests, the LSWT is capable of utilizing the High Attitude Robotic Sting (HARS). HARS allows for a sting mounted model to be maneuvered from -15° to +95° in pitch, -360° to 360° in roll, and -45° to 180° in yaw.

2.2   Facility Modifications

The purpose of this thesis is to outline the modifications made to the LSWT to increase the maximum obtainable dynamic pressure in the test section. This section will serve as an overview of these modifications which will be explained in more detail in Section 4.

The current configuration including the 7 x 10 ft test section is capable of achieving a dynamic pressures ranging from zero to 120 psf (220 MPH). The goal is to achieve a dynamic pressure equivalent to Mach 0.4 (nominally 240 psf). In order to accomplish this task, the test section was reduced from the current 7 x 10 ft with

1 ft chamfers, to a square 7 x 7 ft. This change also necessitated a new diffuser to transition from the reduced test section size to the existing concrete diffuser. This new diffuser measures 304 inches in length (just over 25 feet) and spans the vertical height of the concrete diffuser.

Because the original diffuser is only 46-feet-long, staying below the recommended maximum diffusion angle of $\theta_{eq} = 3.5°$ (From Barlow[6] citing Bradshaw et al.[7]) with the 7 x 7 ft test section would not be possible. To combat this problem, a vertical splitter plate was installed running 336 inches (28 feet) from just inside the exit of the test section, to 45 inches aft of the new diffuser. The splitter plate also helps avoid separation issues when a model may be shedding separated vorticies. The final design can be seen in Figure 2.2 where the existing structure is made to be translucent.
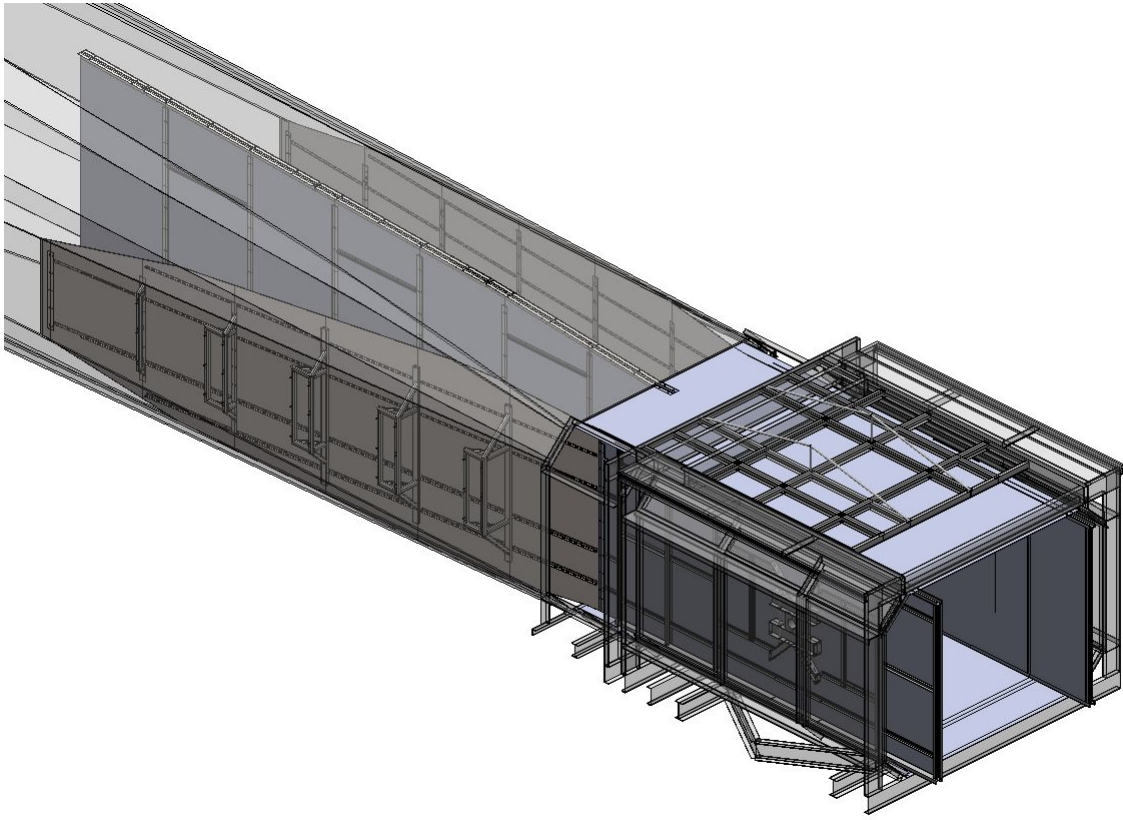
Figure 2.2: Final test section and diffuser design.

The final addition to the LSWT is a new expansion joint seal on the back leg of the circuit. The current expansion joint was not rated for the high pressure loads achieved when running at the new top speed. To reduce the risk of a structural failure, the expansion joint was reinforced with eight, 1.0 inch steel tensioning rods placed on the exterior flange of the wind tunnel. In addition to the tensioning rods, the seal was upgraded to a more robust rubber compound and a rolled over design, as seen in Figure 2.3, to maintain an environmental seal even at high expansion.
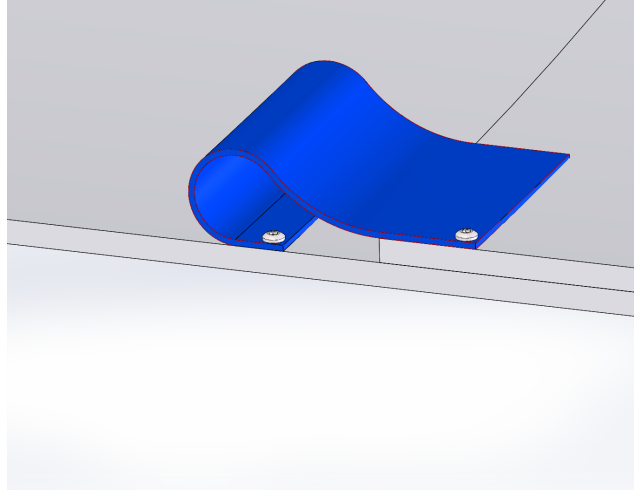
Figure 2.3: Rolled-Over Expansion Joint Seal

2.3 Testing Procedures

The flow speed is controlled using feedback from a differential pressure across the contraction cone, q_{set}. The corresponding dynamic pressure in the center of the empty test section, q_{act}, is calibrated against q_{set} for a specific test section geometry. When the tunnel is in operation, q_{set} is measured and controlled to maintain q_{act} within 0.2% or 0.15 psf of desired value, whichever is larger.

The temperature inside of the test section is measured using a thermocouple located on the wall at the entrance to the test section. Barometric pressure is measured and recorded from the balance room located beneath the test section. Test section static pressure is measured via a pitot-static tube located on the east wall of the test section. These measurements allow for calculation of the test section flow speed at each data point.

During testing, measurements of flow conditions can be made at various points by use of the traversing mechanism (TM) described in Section 2.1. The TM is equipped with a pitot-static probe attached to a ESP-32HD differential pressure transducer.

Each differential pressure transducer is calibrated every three months through a linear calibration routine spanning the full range of the scanner. In addition to this calibration, each run takes a wind-off zero point before and after the data is taken to perform a linear interpolation of the zero-pressure offset voltage to account for temperature changes during the run. An example calibration file can be found in Figure 2.4.
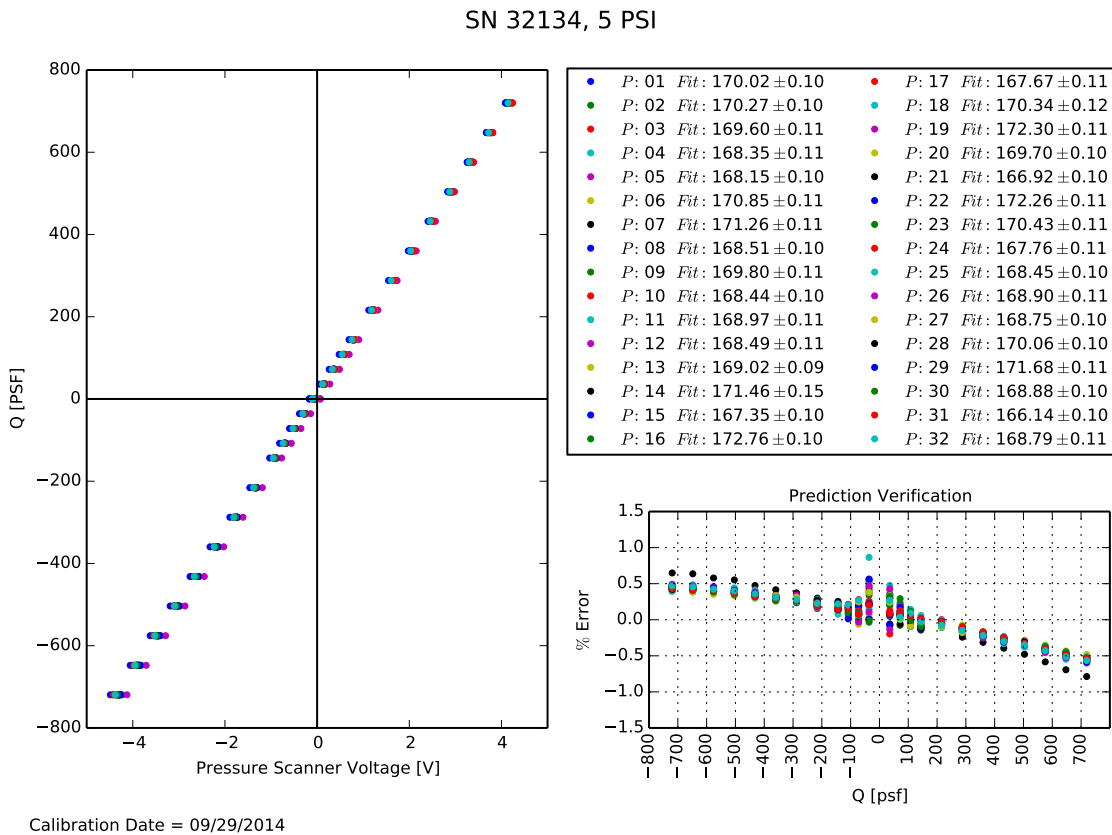
Figure 2.4: Calibration Curves for an Example 5 PSI Differential Pressure Transducer

3. THEORETICAL ANALYSIS

While both Sahoo[4] and Guthery[1] predicted that Mach 0.4 would be possible given the correct set of conditions at the LSWT, neither made their predictions with both the new motor limit and the 7 x 7 ft test section constraints. This section will analyze wind tunnel data collected on the existing 7 x 10 ft test section and attempt to make predictions for the 7 x 7 ft case.

3.1 Blade Stall

In May 2012, the LSWT installed a new 3000 HP TECO-Westinghouse electric motor in conjunction with a new Variable Frequency Drive (VFD) which allowed for varying the RPM with which the motor turns. In previous years, the limiting factor on wind velocity was the power required of the fixed RPM electric motor. However, due to the new variable RPM ability, it is possible for the fan blades to stall before the maximum available power is reached. While this is usually avoided by increasing RPM, the 1200 RPM limit and the desire to reach a new maximum speed posed the potential for blade stall at maximum RPM at less than the maximum available power.

In initial theoretical analysis, a first order approach for calculating power required was used. The power required to drive the wind tunnel scales as described in Equation 3.1 where A_{ts} is test section area in ft^2, M is Mach number, and q is the test-section dynamic pressure in psf.

$$\text{Power} \propto\ A_{\text{ts}}M^3 \quad \text{or} \quad \text{Power} \propto\ A_{\text{ts}}q^{3/2} \qquad (3.1)$$

While a fit of Equation 3.1 yields the power required to achieve a specified dynamic pressure with a given test section geometry, neither blade stall nor potential circuit efficiency variations are considered in those calculations. In order to predict blade stall characteristics, a proxy for the angle of attack of the fan blades is needed. For blade stall tests the motor RPM was fixed while blade pitch was increased to increase velocity in the test section. Power required by the motor was monitored throughout the test and plotted against the effective axial velocity at the fan station. Before blade stall, power required follows

$$P_{\text{req}} = P_0 + K q^{3/2} A_{\text{ts}} \tag{3.2}$$

where P_0 is the $q = 0$ power required of the motor (a function of RPM), A_{ts} is the area of the test section, and K is a proxy for the net aerodynamic losses. The proxy K, and P_0 are determined by a linear fit of the stall test data where K is the slope of the fit, and P_0 is the y-intercept.

As seen in Figure 3.1, the true angle of attack of the fan blades, α, is represented by the difference in the geometric angle of attack, α_{geo}, and a relative angle of attack represented by an advance ratio of $V_{\text{fan}}/R\omega$ where the advance ratio is found by

$$\frac{V_{\text{fan}}}{R\omega} = \frac{V_{\text{ts}} A_{\text{ts}}}{R\omega \; A_{\text{fan}}} = \frac{A_{\text{ts}}}{R^3 \omega \pi} \sqrt{\frac{2q}{\rho}} \tag{3.3}$$

Figures 3.2 and 3.3 show the data from the stall tests. Figure 3.2 was used to determine the efficiency K and P_0, where Figure 3.3 shows the location of stall for various RPMs. For a preliminary model of blade stall, only the advance ratio of $V_{\text{fan}}/R\omega$ will be used for prediction. In future sections a more detailed model will be refined from data.
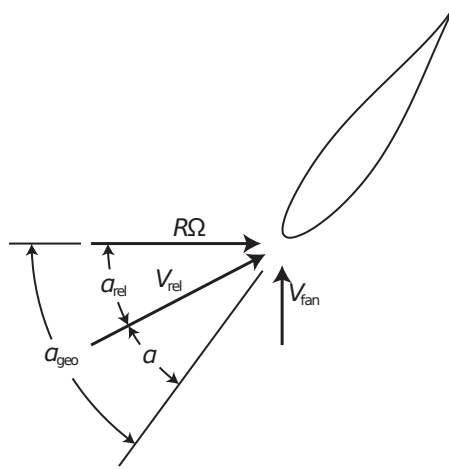
Figure 3.1: Angle of attack of the fan blades
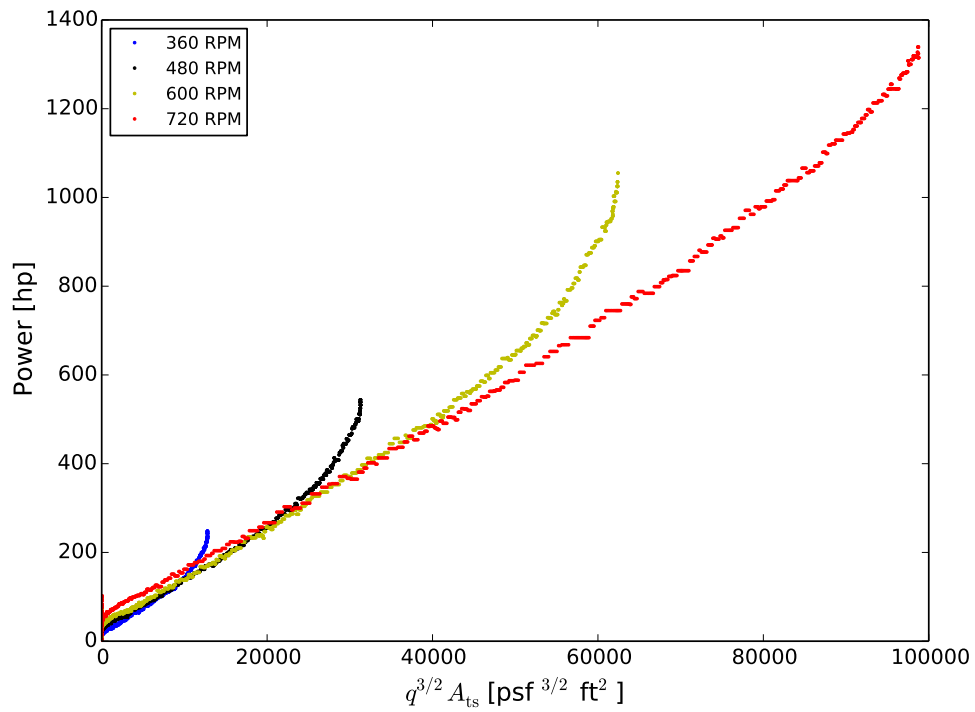
Figure 3.2: Net aerodynamic loss and zero-q power offset
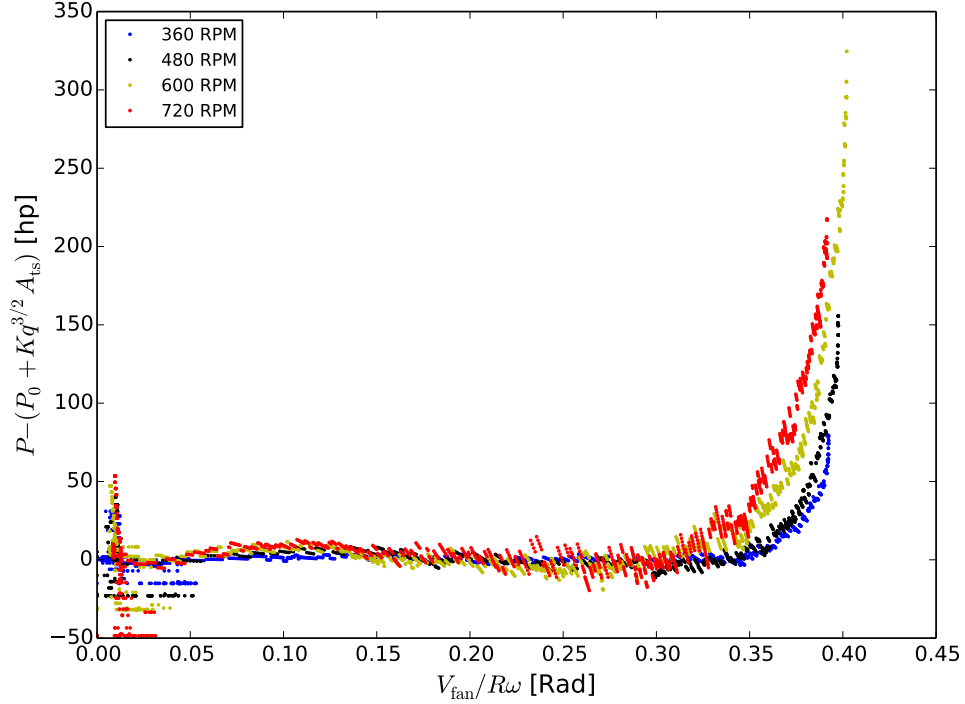
Figure 3.3: Fan stall results

From Equation 3.3 for a test section area of 49 ft^2 and 1200 RPM motor setting, it was determined that blade stall would not occur until approximately 620 psf, well beyond the 240 psf nominally required for $M = 0.4$.

3.2 Power Predictions

In addition to the predictions on blade stall, it is important to ensure the power available is sufficient to achieve Mach 0.4 for an empty test section. As shown in Figure 3.2 and Equation 3.1, the power required by the motor to achieve a set dynamic pressure in the test section scales with $q^{3/2}A_{\text{ts}}$. When in the non-stalled region, this relationship yields a linear model for power given in Equation 3.2. Figure 3.4 shows this relationship extrapolated out to $M = 0.4$ with $A_{\text{ts}} = 49$ ft^2 and $q = 240$ psf. This gives an initial prediction of power required to achieve $M = 0.4$ of 1979 HP

for the 960 RPM case. In order to avoid excess vibrations, a motor rotation speed of 960 RPM was selected rather than the more efficient 1200 RPM. It is noted that the efficiency of the new diffuser, K, is assumed to be constant with RPM from the concrete diffuser. In actuality, due to the reduced θ_{eq} of the new diffuser design, K is expected to be more efficient.
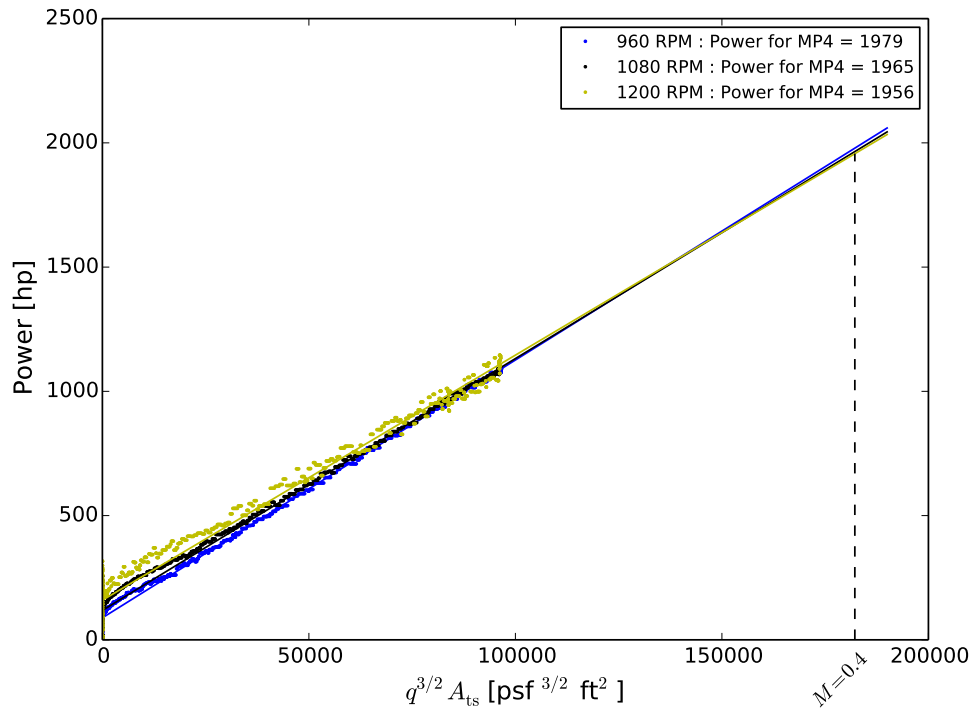
Figure 3.4: Prediction of power required from 7 x 10 ft test section blade stall tests

Due to length constraints on the diffuser, it is known that a splitter plate will be necessary to achieve the optimal diffusion angle of $\theta_{eq} \leq 3.5°$. This vertical splitter plate will introduce skin friction drag to the tunnel system which will require additional power to offset. Equation 3.4b outlines the additional power required from an object with known drag where A_{ref} is a reference area of the body and C_F is the

skin friction coefficient. Equation 3.2 is modified for the additional power needed to become Equation 3.5. The diffuser splitter plate will be defined as a flat plate with $C_F = 0.005$ and reference area $A_{ref} = 500$ ft^2 equivalent to the wetted area of the splitter plate. Furthermore, the skin friction calculations of the splitter plate will be done assuming the entire splitter plate is exposed to $q = 130$ psf, the approximate velocity at the half way point of the splitter plate. Utilizing Equation 3.4b yields an estimated additional power of 196 HP for Mach 0.4 in the 7 x 7 ft test section.

$$\Delta P_{req} = Drag \cdot V_\infty = C_F q A_{ref} \sqrt{\frac{2q}{\rho}} \tag{3.4a}$$

$$\Delta P_{req} = q^{3/2} A_{ref} \ C_F \sqrt{\frac{2}{\rho}} \tag{3.4b}$$

$$P_{req} = P_0 + q^{3/2} A_{ts} \left(K + \frac{A_{ref} \ C_F}{A_{ts}} \sqrt{\frac{2}{\rho}} \right) \tag{3.5}$$

With the addition of the new diffuser splitter plate, the power required to achieve $M = 0.4$ has increased from 1979 HP to an estimated 2175 HP. It is important to note at this point that current limitations from the electric utility provider at the LSWT reduce the available motor output from 3000 HP to 2400 HP at night, and only 1600 HP in the daytime. As seen above, the estimate for the power required to reach Mach 0.4 is below the nighttime limit of 2400 HP.

4. WIND TUNNEL PHYSICAL MODIFICATIONS

Section 2 briefly discussed the LSWT in both the conventional 7 x 10 ft test section configuration and the new 7 x 7 ft configuration. This section will expand on the design and build of the new 7 x 7 ft configuration.

4.1 Contraction and Test Section Design

The 7 x 7 ft test section design presented here is of a previously manufactured contraction cone and test section which was first designed and implemented by Sahoo[4] in 2008.

The contraction section provides a transition between the current concrete contraction cone and the new 7 x 7 ft test section. The new contraction section is a bolt-on-addition to the current concrete contraction cone. This bolt on section is comprised of ⅛ inch thick aluminum sheets which were attached to 1x½ inch steel c-channel by means of #8-32 flat-head socket cap screws. All bolts were countersunk and taped to minimize wall roughness and skin friction. The steel and aluminum assemblies were attached to the concrete using ⅜-16 socket head cap screws into adhesive-grip internal thread concrete anchors. This anchoring system provides a permanent mounting point within the concrete walls.

The test section is comprised of 12 unique panels each of which is an assembly of steel c-channels and 3⁄16 inch aluminum sheet. Each of the panels were made with 2x1 inch steel c-channel for a frame, with the exception of the third panel on each side, which was made with 5x1¾ inch steel c-channel. The reason for the more robust structure on the third panel was the test article for the original design mounted through this panel. Sahoo[4] was creating a facility which could test dynamic stall on helicopter blades, and as such would see extremely large loads during testing. The

¾₁₆ inch aluminum sheets are attached to the steel frame by means of #10-32 flat-head socket cap screws which are countersunk and taped over similar to the contraction section's hardware. Each panel assembly attached to the next via ½ inch steel hex head bolts. The entire assembly is connected to the existing test section floor and ceiling with ½ inch steel hex head bolts with their corresponding nuts either below the floor in the balance room, or above the test section roof. The fifth panel on each side has an adjustable vent which allows for control of the static pressure within the wind tunnel. The sixth panel on the West side has a removable door to allow access to the test section for model changes or viewing when the tunnel is not in operation. An example panel frame structure can be viewed in Figure 4.1
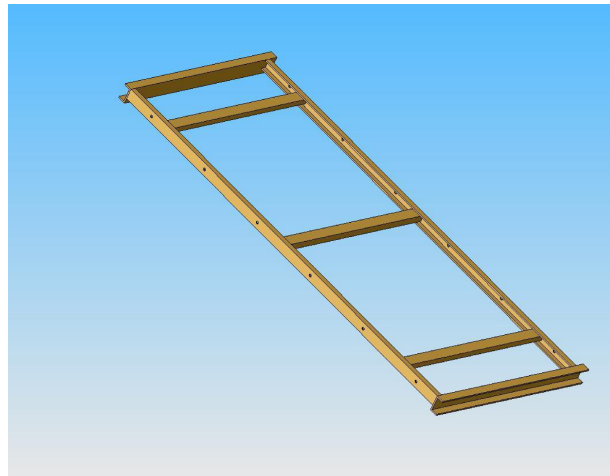
Figure 4.1: Example wall panel structure [4]

Special care was taken when designing the 7 x 7 ft test section to allow for modifications to view a model for Particle Image Velocimetry (PIV). As such, there are viewing windows on the east wall's third panel for use in 2-D PIV, and in the 2nd and 4th panel on the west wall to allow for stereoscopic PIV.

In addition to the wall panels, a new roof was designed and built to interface with the 7 x 7 ft test section. This roof is made primarily of 3x2½ inch steel I-beams. These I-beams are covered with the same 3⁄16 inch aluminum sheets used for the wall panels. This roof serves to transfer some of the loads from the model to the wind tunnel structure. On the roof there are two circular holes through which a light or laser can be mounted for use during a test. If either of these holes are not in use, an aluminum cover can be put in place to prevent flow out of the test section. The roof can be seen in Figure 4.2

Figure 4.2: Drawing of 7 x 7 ft roof structure [4]

4.2 Diffuser Design Considerations

Originally, Sahoo[4] designed a 10 foot long diffuser as an interface between the new 7 x 7 ft test section and the concrete 7 x 10 ft diffuser. This diffuser design required the addition of a series of vortex generators in order to combat separation due

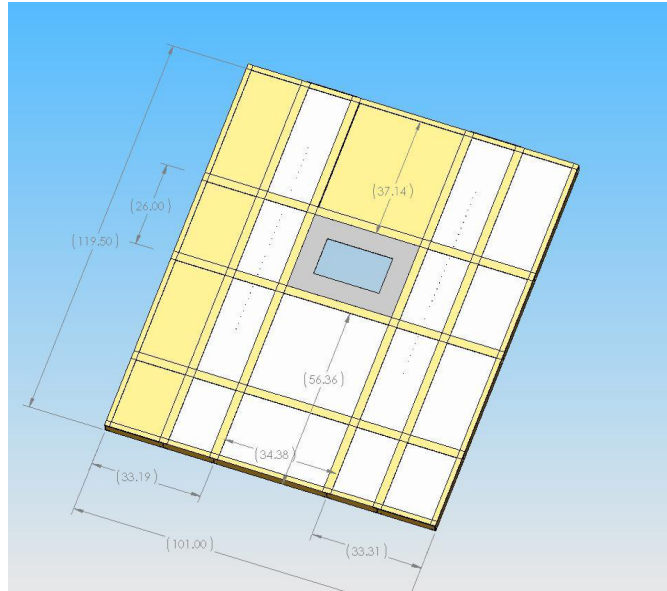to the extreme diffusion angle. Sahoo predicted with a 7 x 7 ft test section, and current power restrictions that Mach 0.4 would be possible. However, after installation the maximum achievable Mach number was a nominal 0.28. The difference in the theoretical and actual maximum Mach number was attributed to diffuser efficiency, and to a lesser extent, power available.

The LSWT has since upgraded its motor from the fixed RPM 1250 HP maximum electric motor to a TECO-Westinghouse 3000 HP electric motor with a Variable Frequency Drive (VFD) system. This new system removed the power limitations seen by Sahoo leaving only the issue of diffuser efficiency to tackle.

As we have shown in Section 3, reaching Mach 0.4 is theoretically possible with the power and test section geometry available at the LSWT. The next steps are to design and build a diffuser which removes the limitations observed by Sahoo. As mentioned in Section 2.2, Barlow[6] cites Bradshaw et al.[7] as recommending a maximum equivalent expansion of $\theta_{eq} \leq 3.5°$. This equivalent expansion angle as defined by Guthery[1] as

$$\theta_{eq} = \arctan\left(\frac{1}{2}\frac{D_{h2} - D_{h1}}{L}\right) \tag{4.1}$$

Where D_{h1} and D_{h2} are the hydraulic diameters of the entrance and exit of the diffuser respectively, given by

$$D_h = \frac{4A}{P} \tag{4.2}$$

and L is the length of the diffusion section measured at the centerline. For Equation 4.2, A is the cross sectional area of the duct, and P is the perimeter.

For the LSWT the entrance geometry is 7 x 7 ft, square cross section which correlates to a $D_{h1} = 7.0$. However, because a vertical splitter plate will be used,

the equivalent entrance geometry is 7 ft x 3.5 ft with $D_{h1} = 4.67$. The exit geometry varies with L. It was determined that a diffuser of length $L = 304$ inches with a vertical splitter plate, which creates a $D_{h2} = 6.84$, would be sufficient. Using Equation 4.1 yields $\theta_{eq} = 2.45°$.

The design of the new diffuser allowed for the implementation of lessons learned from the original design by Sahoo. It was important to maintain ease of install and uninstall as this diffuser has the potential to be used multiple times per year. The current rate of 1.5 days to install the 7 x 7 ft test section without the diffuser does not allow for a large section of time for this process. As the goal was to maintain less than three days total for a complete installation the following requirements were set forth:

- All fasteners must be accessible by a single person standing in the current diffuser

- No individual piece of the diffuser should weigh more than 80 lbs

- Common parts should be used wherever possible

- At no point during installation should it be necessary for more than two individuals to carry or hold a part

- All parts should be transportable by human power as no hoist system is available

- Adjustability for unknown geometry must be maintained

These design requirements are maintained with only a small number of exceptions in the final design. While the design did require more difficult machining tolerances, the outcome is a product which can be relatively easily used. This ease of installation will make up for the initial extra cost of machining.

4.3 Diffuser Wall Design

The new diffuser requires three main components, two diffuser walls discussed here, and a single vertical splitter plate discussed in Section 4.4. The wall panels provided a unique challenge to design as the current concrete diffuser does not have an accurately known geometry. While there has been a 3-D CAD model for many years, small deviations are common and require attention during the design phase.

In order to meet the design requirements outlined in Section 4.2 a modular structure was adopted. The octagonal cross section of the concrete diffuser was known to have a vertical wall section which at a minimum was 38 inches in height. It was decided that this vertical section would be the primary mounting point for the entire diffuser wall. This decision allowed for the avoidance of many of the variable geometries of the concrete diffuser. In addition to the decision to mount only to the vertical surface, a vertical wall was adopted which would change height to match the varying geometry of the diffuser. This approach was chosen rather than a curved face for ease of manufacture and reduction of structural weight.

Because the entrance geometry was known, and the overall length was set at 304 inches, the face and geometry of the new diffuser wall can be approximated from the CAD model of the concrete diffuser. This wall geometry can be seen in Figure 4.3.
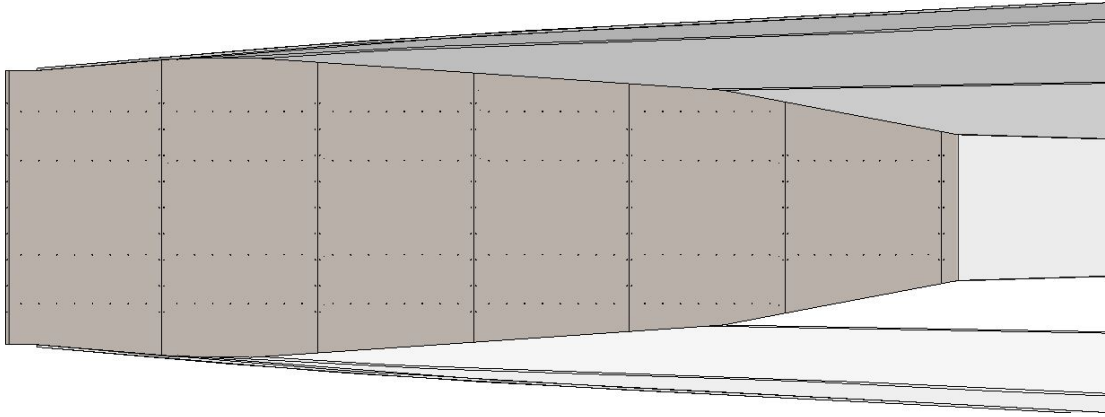
Figure 4.3: Diffuser wall geometry as seen inside concrete diffuser

Although the static pressure difference across the diffuser wall panels is negligible, the potential for panel flutter and other unsteady effects remains a concern. Because of this, the walls were to be made out of ¹⁄₁₆ inch steel sheet. This would allow for the strength necessary, while still maintaining some weight considerations. This sheet is readily available in 4 x 8 ft sections, which is why the diffuser was designed for a total of six full sheets with a seventh small addition. It was also decided at this point that the addition of angle iron stringers was necessary to combat wave propagation in the sheet down the length of the diffuser. The angle iron selected for this task was 1⅛x1⅛x⅛ inch thick steel angle iron. These stringers would run length wise down the diffuser sheets to add support. While welding was an option for attaching these stringers, the ultimate design choice was to use ¼-20 button head cap screws with corresponding nylon locking nuts to ease manufacture and allow for removal and replacement should an issue arise in the future. Although this decision did lead to a larger number of bolt heads exposed to the flow, their effect on flow quality in the test section was not significant.
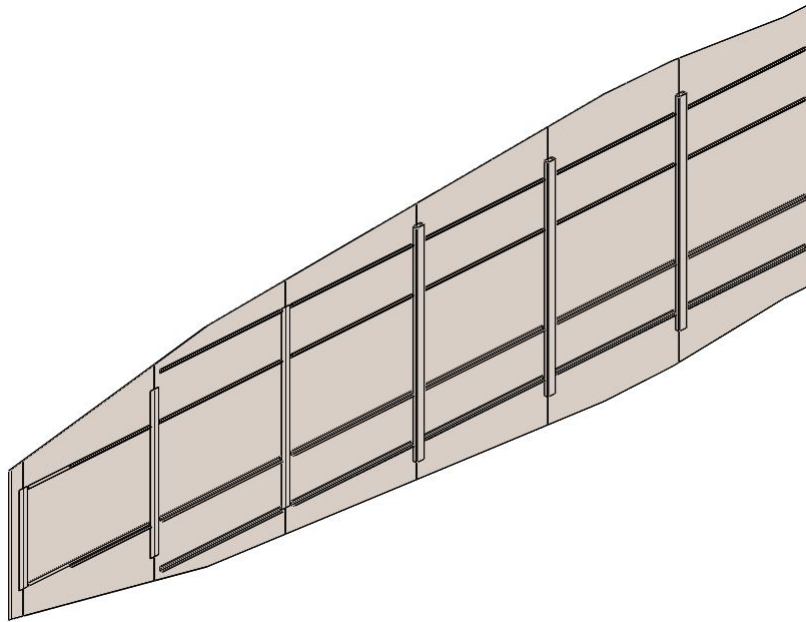
Figure 4.4: View of back side of diffuser wall with stringers visible

In order to attach the wall panels to the current concrete diffuser a structural member is needed. In keeping with the design requirements, a structure which used a common design with only scaled components was decided on. The need for scaling in some directions was necessary because, as the diffuser extends in length the proximity to the concrete increases, thus reducing the space available to mount a structure.

Steel was selected again as the material of choice due to its ease of welding. 2x2x⅛ inch square tubing was decided on for the bulk of the structure, while either 3x1.5x⅛ inch rectangular tubing, or 3x⅛ inch flat bar was selected as the interface between the structure and wall panel. The reason for the increase from 2 inches to 3 inches area for the interface was due to the structure needing to span the gap between two wall panels. Due to the inherently inaccurate installation procedure of the 7 x 7 ft test section and unknown nature of the concrete interface, the larger area in which to mount was crucial. It was also decided at this point that installation would begin

at the test section and work downstream. This caused a design decision that each structure should be able to be placed while upstream components are already in place. Because of this design decision the final structural components were designed with all fasteners being either in-line with the panel gap, or downstream of it.

The first four structural components were designed as a 36x12 inch rectangular structure with horizontal supports running towards a vertical interface made from either rectangular tubing or flat bar. This design allowed for changing the length of the horizontal supports to adjust for proximity to the wall. The drawback to a design like this is the need for a machined edge on the welded interface between the vertical rectangular tubing and the horizontal support structure. This machined edge serves to set the equivalent diffusion angle θ_{eq}. The structure can be seen on the left in Figure 4.5.

Figure 4.5: Structure 1 and Structure 5 of the diffuser wall panels

Each of the first four structures on either wall incorporated an identical rectangular assembly, as well as similar vertical supports. By maintaining structural similarity, a single jig can be made for the welder, reducing manufacture time and difficulty.

The fifth structure is comprised of a single vertical square tubing member with horizontal supports leading to the vertical 3x⅛ inch flat bar. This structure has additional holes through the flat bar to allow access to the mounting hardware.

The supports attach to the concrete diffuser using ⅜-16 socket head cap screws into adhesive-grip internal thread concrete anchors. A total of six bolts hold each of the first four structures onto the wall with the fifth being held on by only three. The final three anchor points are at the interface of the sixth and seventh panel behind which there is no structure, only anchor points to the wall. In addition to the bolts, six ½-13 set screws were used to add adjustability in diffusion angle, vertical orientation and distance from the wall. The adjustability in the downstream direction was achieved by using over-sized through holes for the attachment bolts, allowing for sliding in any direction. It is important to note that the downstream side of any support structure does not come into direct contact with the concrete diffuser, but is instead held off by the set screws defining the angle between the wall and structure.

Each support structure attaches to the steel wall panels by means of ¼-20 button head cap screws. These are inserted into threaded holes on the structure itself. The decision to use threaded holes was necessary because of inaccessibility after the panel is lifted into place.

The design of the diffuser wall panel is such that there is no initial distinction between either of the two walls. However, because customization is necessary to insure a proper fit, once installed, the two walls will then be unique and non-interchangeable.
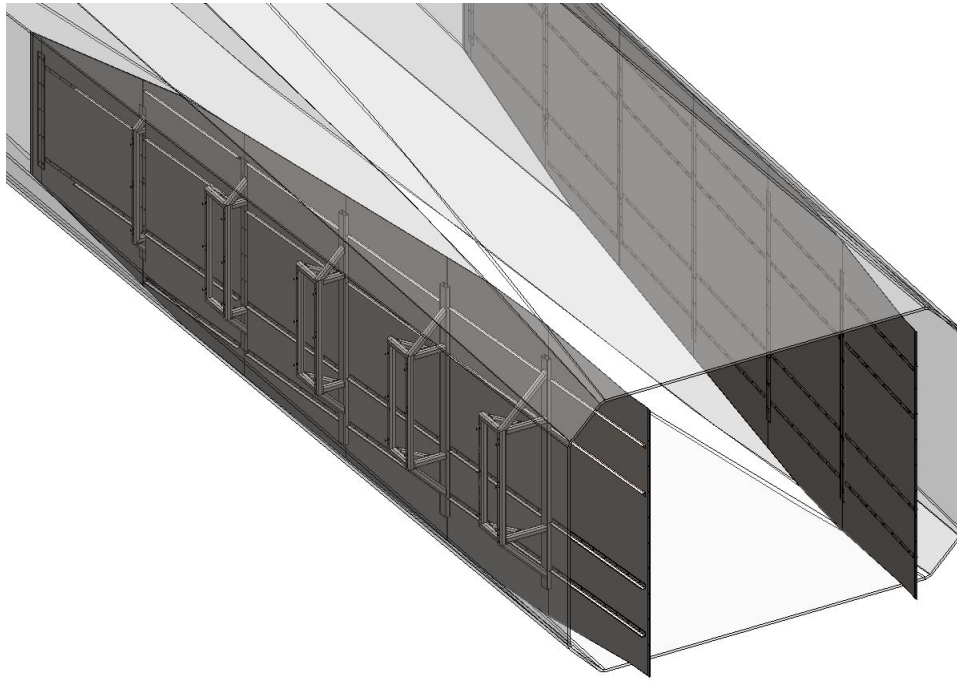
27

Figure 4.6: Wall assemblies inside of concrete diffuser

4.4   Splitter Plate Design

The short diffuser length requires a splitter plate to maintain an equivalent diffuser cone angle below 3.5°. The design of the splitter plate posed unique challenges as there was no existing structure to support such a large wall, and the height requirements made single sheet construction uneconomical.

In order to save on cost and increase structural rigidity without the need for numerous stringers and ribs, the bulk structure for the splitter plate was made to be ¾ inch cabinet grade plywood sheets measuring 4x8 feet. Cabinet grade was chosen for the more uniform surface, higher quality wood which lead to less variation in internal structure, and accurate ¾ inch dimensions.

As the height requirements of the splitter plate exceeded the 8 foot maximum sheet length of plywood after the first 4 feet, multiple sheets stacked on top of one

another are necessary. These splits were designed to stagger across the downstream length of the splitter plate. This decision was made so each split was supported by full sheets of plywood on either side. In addition to the plywood support, a set of four 1⅛x1⅛x⅛ inch thick steel angle iron pieces were fastened into a cross configuration using ¼-20 button head cap screws and corresponding nuts. This cross support increased the stiffness of each joint to avoid buckling in highly separated wind loads. Figure 4.7 shows the plywood sheet configuration down the splitter plate.
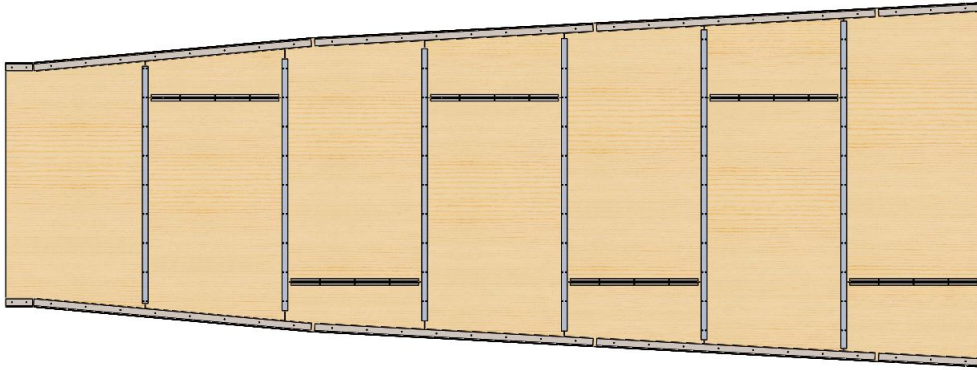

Figure 4.7: Splitter plate with mounting and support hardware

The divisions between the vertically stacked sheets are reinforced with a set of 3x⅛ inch steel flat bar attached to 2x¾x⅛ inch thick aluminum extruded t-bar. This structural set gives additional buckling stability which further reinforces the horizontal plywood split. This structural support package can be seen in Figure 4.8. Here, the ¾ inch web of the t-bar can be seen to pass between the plywood sheets, and is fastened by ¼-20 button head cap screws. This is a different system than is used for the horizontal split where the plywood sheets are in contact.
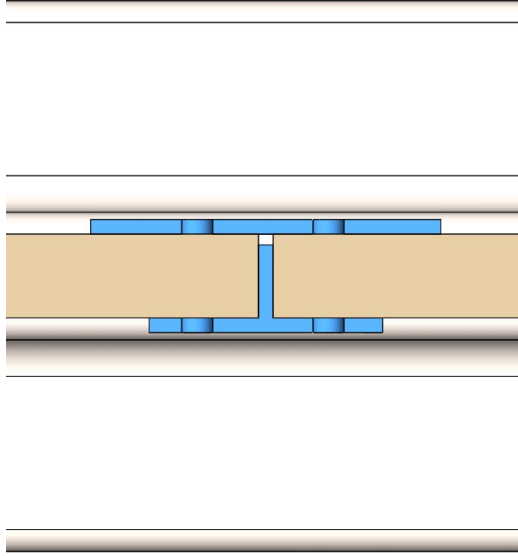
29

Figure 4.8: Detail view of t-bar support system

In order to maintain consistency between the diffuser wall panels, contraction cone section, and the splitter plate, the attachment to the concrete section of the existing wind tunnel is by means of ⅜-16 socket head cap screws into adhesive-grip internal thread concrete anchors. These anchors fasten to 3x2x³⁄₁₆ inch thick steel angle iron. The 3 inch web of this angle will sandwich the plywood splitter plate sections with ¼-20 button head cap screws and corresponding nuts. This allows for the entire system to be tensioned by first securing the large angle iron to the plywood, followed by tightening of the ⅜-16 bolts. This tension will limit the ability of the plywood to flex under oscillatory load. A view of the entire assembly with hardware can be seen in Figure 4.7. Finally, Figure 4.9 gives a view of Figure 4.6 with the splitter plate installed.
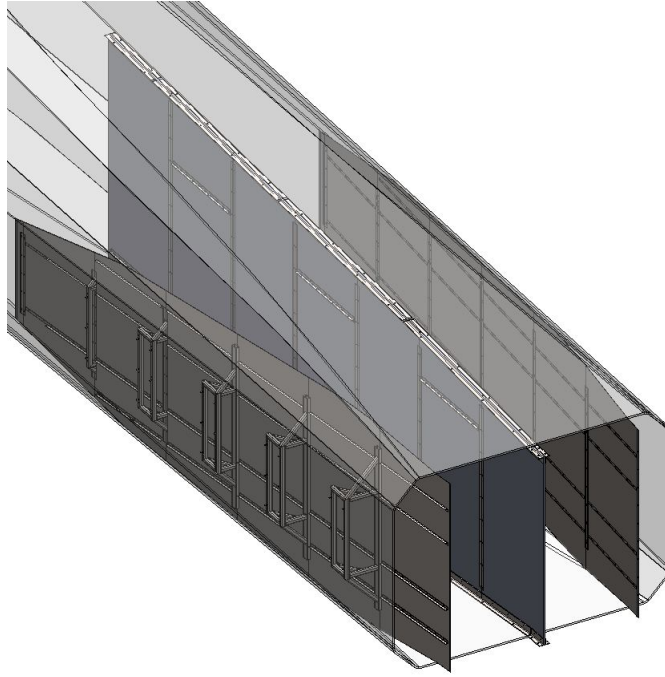
Figure 4.9: Full diffuser wall and splitter plate assembly in existing concrete diffuser

4.5   Expansion Joint Design

The final major design portion required to reach M=0.4 is the far side expansion joint. While the LSWT has three expansion joints to allow for movement of the structure during runs, the joints at the fan and contraction cone are more-or-less fixed in place due to age and deterioration. The expansion joint on the far side, between turns two and three, however, is free to move. With the increase in dynamic pressure needed in the test section to reach M=0.4, the static pressure felt in the large diameter portions of the tunnel are increased as well. Due to this increase, it is necessary to strengthen the expansion joint to avoid excess separation.

The expansion joint is supported in place by two W10x33 steel structural I-beams. These beams are fixed in concrete at the base and welded to the tunnel walls on top. A run up to the maximum dynamic pressure for the 7 x 10 ft test

section was performed and a model of expansion travel determined from that data. Figure 4.10 shows the findings of that run. It was determined that approximately 30 psf was necessary to overcome the initial static friction, and above that value, each additional 70 psf resulted in approximately 1.0 inch of travel. The hysteresis seen in Figure 4.10 is due to the need to overcome friction when contracting the expansion joint. Finally, the approximate 1 inch jump for the last measured data point was due to binding in the joint before becoming fully contracted. To minimize this binding effect grease zerks were added around the expansion joint.
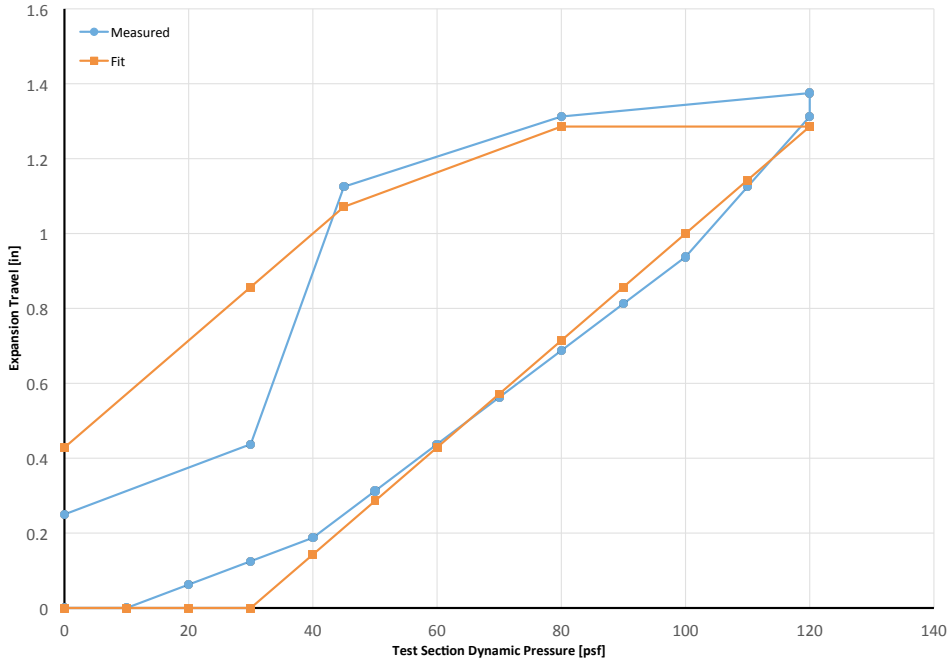

Figure 4.10: Expansion joint travel before added structure

With this model in hand, the addition of structure to restrict the motion of the expansion joint was necessary. The decision to limit travel to 1.3 inches, the equivalent expansion of 105 psf test section pressure, was adopted to avoid over expansion. Through analysis of the expected loads, a design which includes additional structure in the form of steel gussets and tensioning rods was selected. The tensioning rods are custom made 1-8x20 inch long 4340 steel bolts mounted through hemispherical swivels to gussets which were added to the existing expansion joint structure.

The gussets are welded to the existing frame are comprised of a 3x2.25x1 inch thick steel plate on either side of the expansion joint with .5 inch thick supporting ribs spanning between the existing tunnel body and expansion joint flange. This gusset can be seen in Figure 4.11
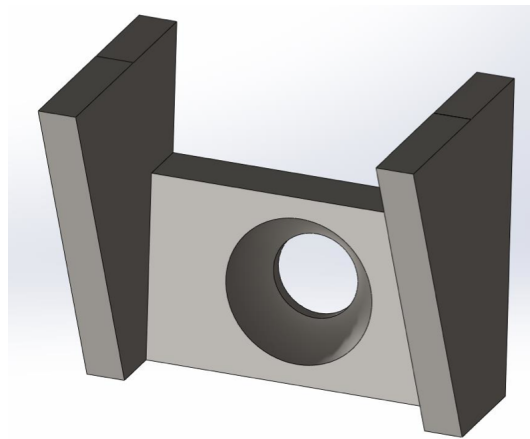

Figure 4.11: Welded on gusset for expansion joint

In total, 10 tensioning rods were used as each was determined to be able to withstand 30,000 pounds in tension. A desired safety factor of 4.5 was used in conjunction with Equation 4.3, where T is the tension per rod in pounds, D is the diameter of the expansion joint, and n is the number of tension rod assemblies.

A safety factor of 4.5 was chosen because of aging materials on the flange. Also, because of friction, expansion is not completely uniform around the joint. This non-uniformity causes some tensioning rods to support more load than others. With Equation 4.3 the tension in each tensioning rod assembly was determined to be approximately 6500 lbf.

$$T = \begin{cases} 0 & : q_{\text{act}} \leq 105\text{psf} \\ \frac{\pi D^2}{4n}\left(q_{\text{act}} - 105\right) & : q_{\text{act}} > 105\text{psf} \end{cases} \tag{4.3}$$

4.6   Installation

Once all components were designed and manufactured, installation began. It was known that some components would have to be custom fit once in the tunnel due to inaccurate tunnel models in the 3D CAD. The first hindrance was found after the installation of the test section panels was complete. While the old drawings showed the test section inserts terminating 9.5 inches before the break of the diffuser, it was found that the panels actually ended 11.75 inches upstream of that point. It was because of this offset that an extension was designed to bridge the gap between the test section wall panels and the first wall panel of the diffuser.

This extension was to be manufactured using the same ⅟₁₆ inch thick steel sheeting over a frame of welded 3x⅛ inch thick steel flat bar, 1⅛x1⅛x⅛ inch thick steel angle iron, and 2x1x⅛ inch thick steel c-channel. The extension was supported from behind by four pieces of 3x2x³⁄₁₆ inch thick steel angle iron which is fastened into the sheet metal roof and floor of the test section. The addition of this extension, while time consuming, did not alter the effectiveness of the diffuser. This was achieved by ensuring that the extension pieces remained parallel to the test section walls. By remaining parallel, the actual diffusion did not begin until its designed location

9.5 inches before the original concrete diffuser break. A rendering of the extension panels, highlighted in blue, can be seen in Figure 4.12.
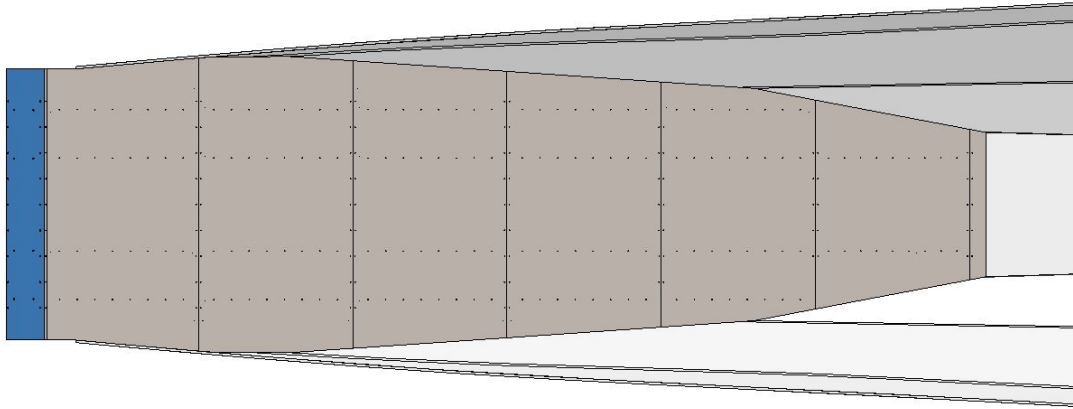

Figure 4.12: Diffuser extension rendering attached to new diffuser design

Once the extensions were manufactured, installation could continue. From this point forward the installation went as planned. It was known that some holes would have to be match drilled to account for tolerance errors on the concrete diffuser, as well as warping of the structural pieces due to welding. However, the only additional change needed was the implementation of two supporting cables which run from the trailing edge of the vertical splitter plate to the concrete diffuser wall. These cables consist of horizontal ⅛ inch steel wire cable attached to turnbuckles which, when tightened, reduce vibration of the trailing edge of the splitter plate. This change was made after observations of the splitter plate at high dynamic pressures exposed a vibration which needed to be removed.

5. FLOW CHARACTERISTIC VERIFICATION

The goal of reaching Mach 0.4 flow speed in the LSWT was made to allow testing in the mid-subsonic range. This range is critical to test a variety of aerodynamic models, including dynamic stall on helicopter blades. This section will seek to verify that Mach 0.4 is possible with the new reduced test section, and verify flow quality at multiple wind velocities.

5.1 Flow Speed Verification

The first verification is a test to determine the maximum flow speed possible for an empty test section. In order to accomplish this, a calibration run was completed which recorded measurements of test section conditions at a rate of 5 Hz. Equation 5.1 is used to determine Mach number from the measured test section conditions, where γ is the ratio of specific heats, taken to be 1.4 for this analysis, P_s is the test section static pressure, and q_{act} is the test section dynamic pressure.

$$M = \left\{ \frac{2}{\gamma - 1} \left[\left(\frac{q_{act}}{P_s} + 1 \right)^{\frac{\gamma - 1}{\gamma}} - 1 \right] \right\}^{\frac{1}{2}} \tag{5.1}$$

Below, Figure 5.1 shows a comparison of Mach number and power required for the high speed run. The maximum Mach number achieved was M=0.408, with a power draw of 2362 HP.
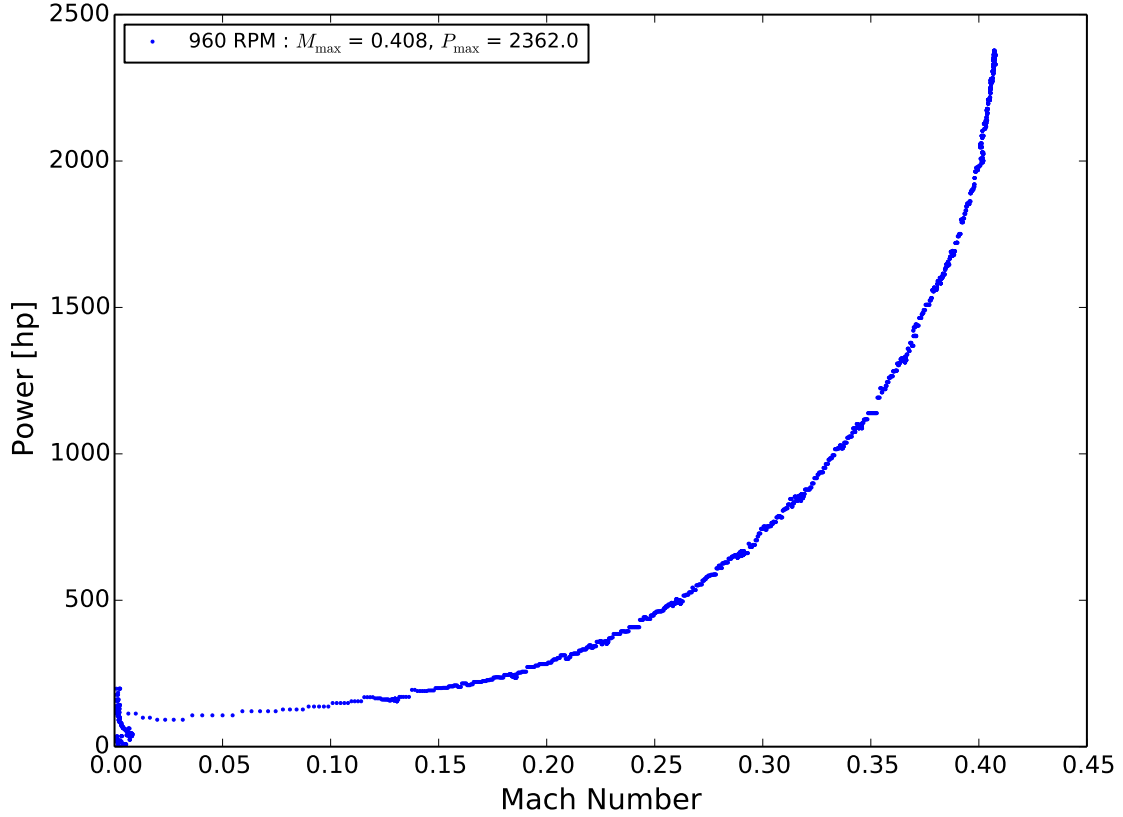
Figure 5.1: Empty 7x7ft test section Mach number vs power required, showing maximum Mach number

5.2   Flow Quality Analysis

While achieving a maximum speed of M=0.4 was demonstrated in Section 5.1, the amount of variation in flow speed throughout the test section is an important second factor. Because of this, various runs were performed to quantitatively show that the flow is uniform throughout the test section. Hidore [5] in 2013 extensively mapped the flow quality of the LSWT in its 7 x 10 ft configuration. He also spent time to map the flow quality around the High Attitude Robotic Sting (HARS) at multiple orientations. In line with Hidore's study, a similar mapping of flow quality was performed in the reduced test section for both an empty test section, and a

HARS installed test section. Due to limitations on time, and installation constraints the HARS study only used a single orientation in-line with the flow.

In the figures below, the LSWT TM system traversed in the Y-Z plane. The X position was centered on the test section's turntable system. The measurements taken of local q_{act} were performed by a Pitot-static probe mounted on the TM arm connected to a calibrated ESP-32HD pressure scanner. Each figure shows the deviation from the mean dynamic pressure measured as a function of position. The test section q_{act} is referenced in the upper left hand corner of the figure.

Figures 5.2 to 5.8, from Hidore [5], show flow quality in the 7 x 10 ft test section for both an empty test section, and HARS installed in-line with the flow.

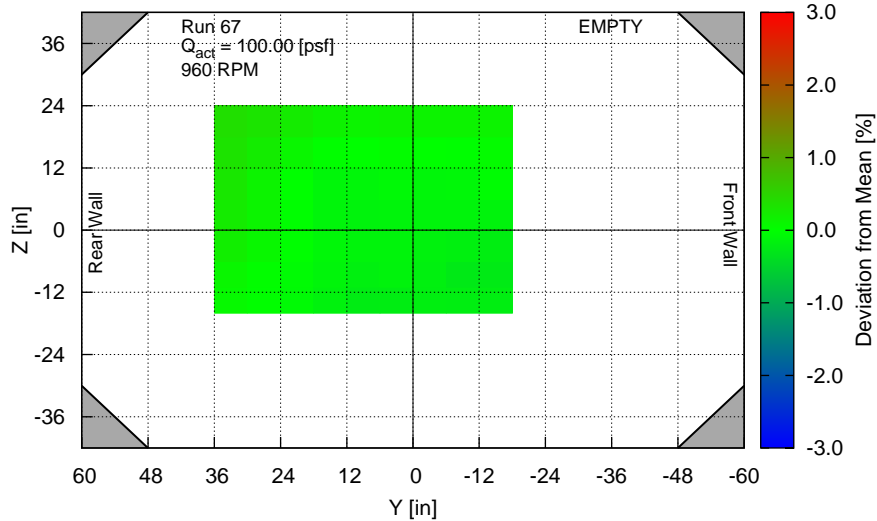

Figure 5.2: Dynamic Pressure Variation at q_{act} of 100 psf, 960 RPM [5]
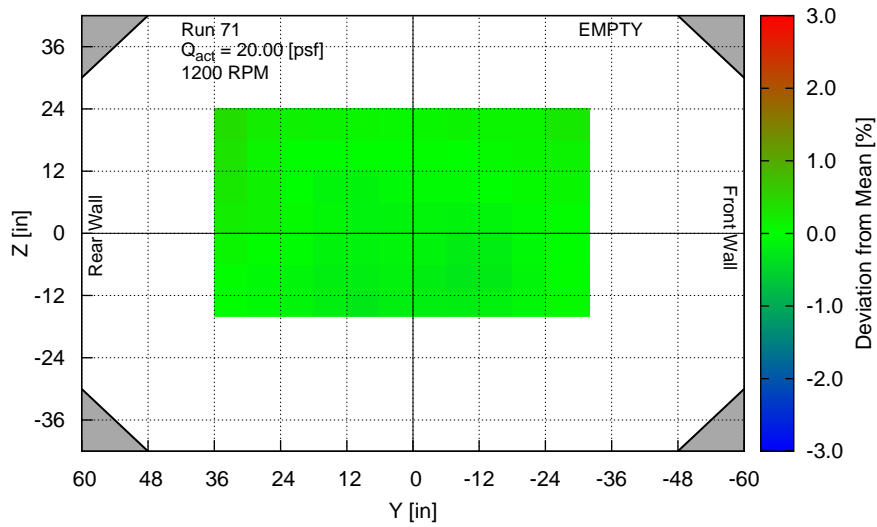
Figure 5.3: Dynamic Pressure Variation at q_{act} of 20 psf, 1200 RPM [5]
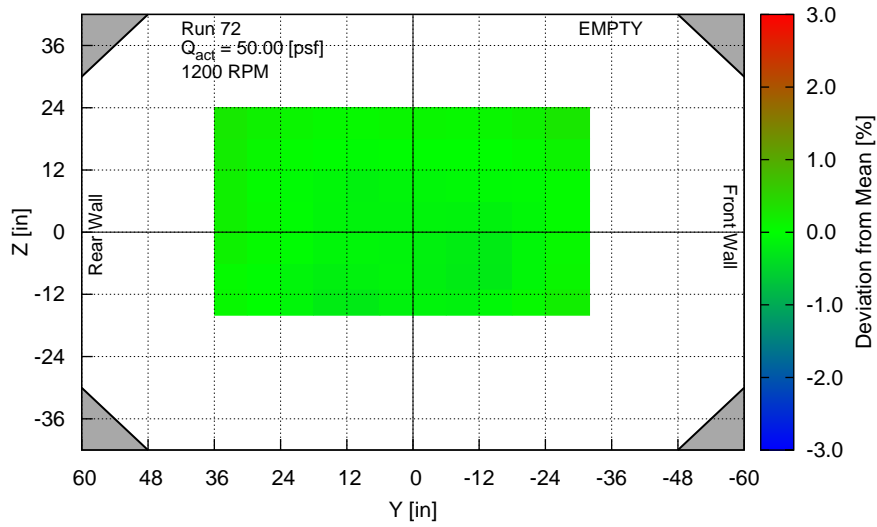
Figure 5.4: Dynamic Pressure Variation at q_{act} of 50 psf, 1200 RPM [5]

Figure 5.5: Dynamic Pressure Variation at q_{act} of 100 psf, 960 RPM with HARS [5]

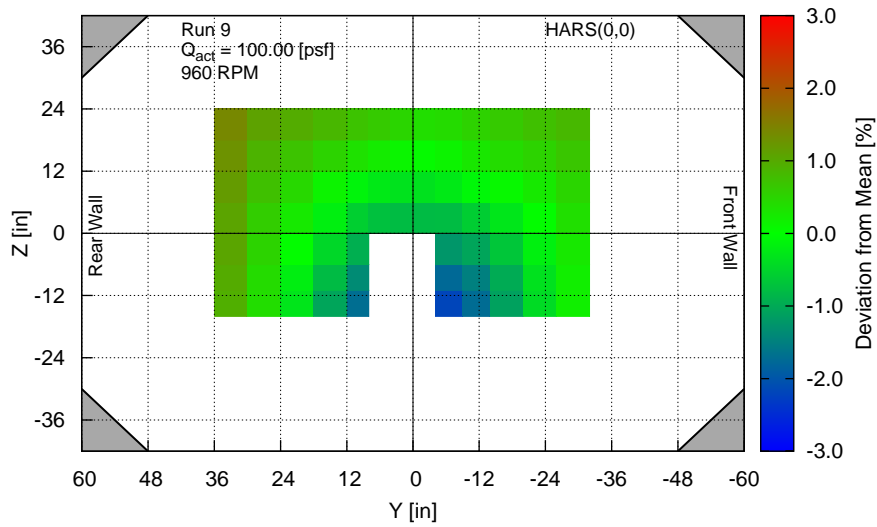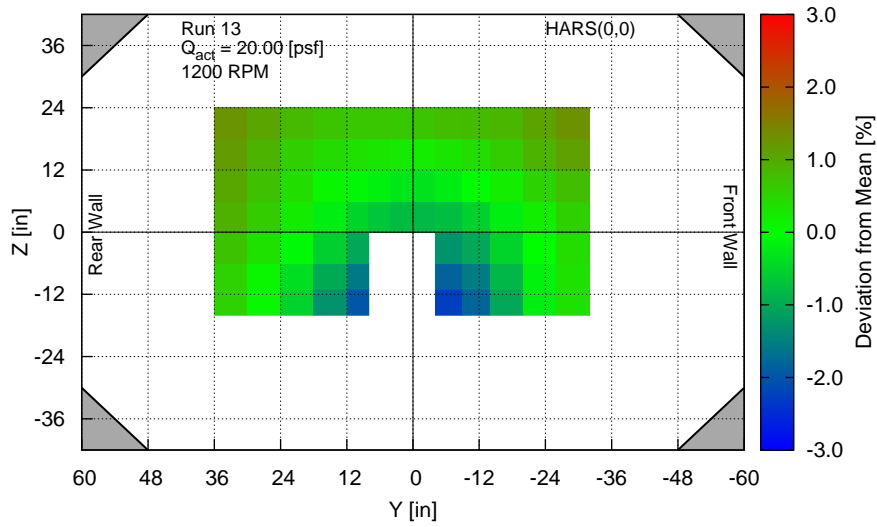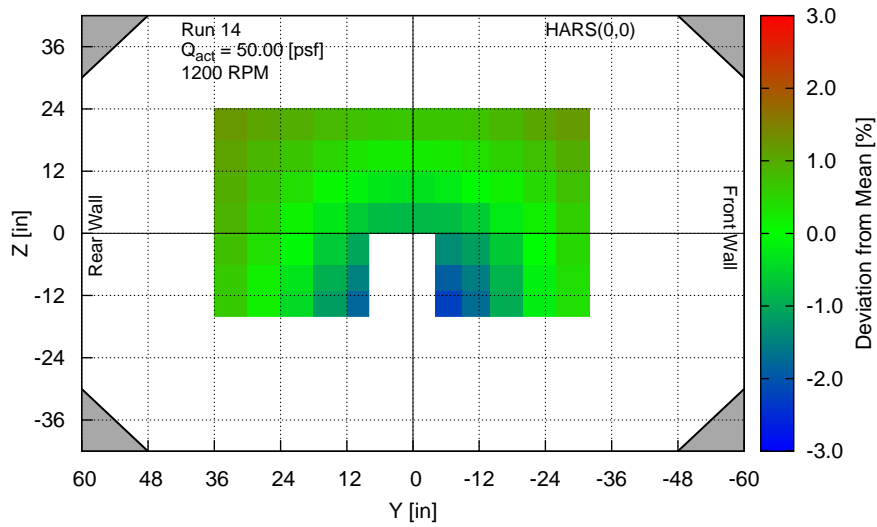Figure 5.6: Dynamic Pressure Variation at q_{act} of 20 psf, 1200 RPM with HARS [5]

Figure 5.7: Dynamic Pressure Variation at q_{act} of 50 psf, 1200 RPM with HARS [5]
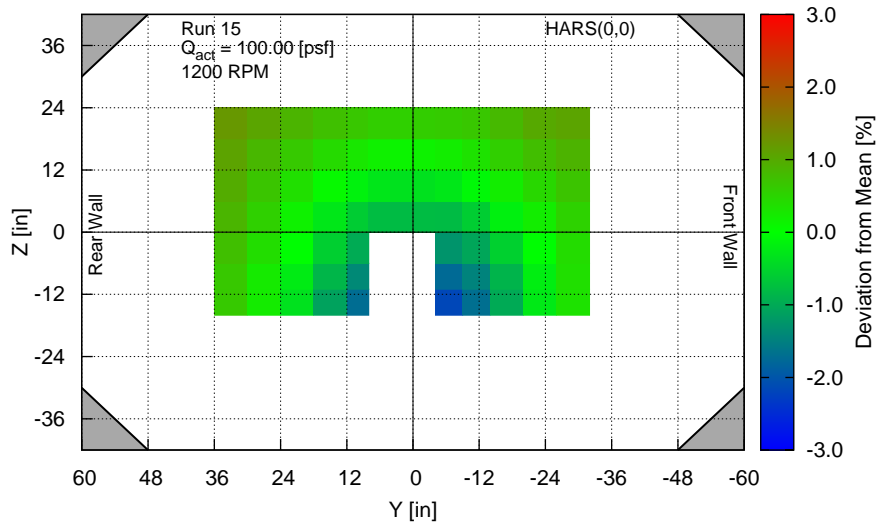
Figure 5.8: Dynamic Pressure Variation at q_{act} of 100 psf, 1200 RPM with HARS [5]

Similar to the figures produced by Hidore, Figures 5.9 to 5.18 show flow uniformity as a function of position. Overall, the 7 x 7 ft test section appears to have improved flow uniformity. Two cases show a relatively large deviation from the mean. However, in each case a repeat of the same flow conditions was performed after the installation of HARS. Hidore concluded that the addition of HARS would cause a decline in flow uniformity. Similar results shown in this test lead to the conclusion that the two deviant cases were not of concern as they were isolated instances which could not be repeated.

Figure 5.9: Dynamic Pressure Variation at q_{act} of 20 psf, 960 RPM, 7x7ft Test Section

Figure 5.10: Dynamic Pressure Variation at q_{act} of 50 psf, 960 RPM, 7x7ft Test Section

Figure 5.11: Dynamic Pressure Variation at q_{act} of 100 psf, 960 RPM, 7x7ft Test Section

Figure 5.12: Dynamic Pressure Variation at q_{act} of 125 psf, 960 RPM, 7x7ft Test Section
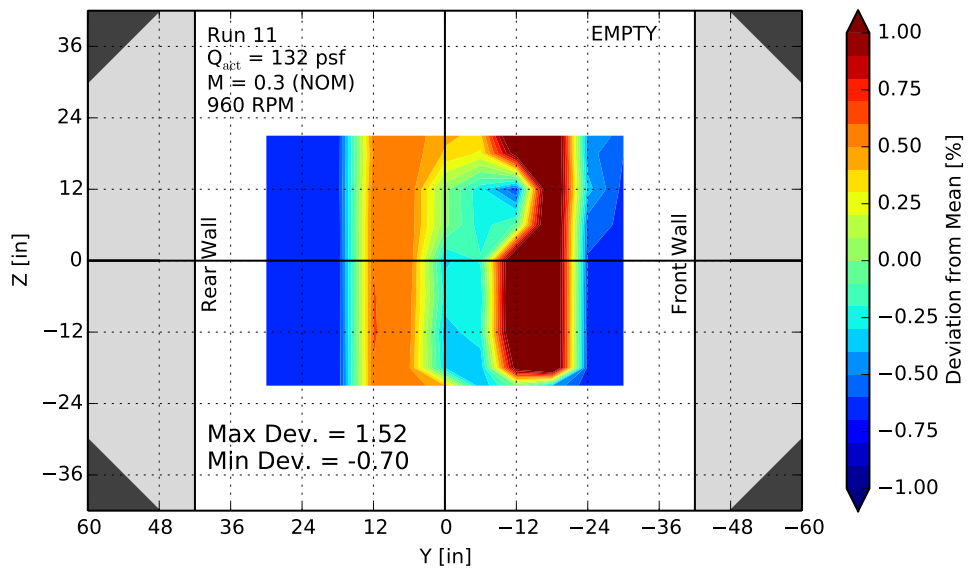
Figure 5.13: Dynamic Pressure Variation at q_{act} of 132 psf, 960 RPM, 7x7ft Test Section
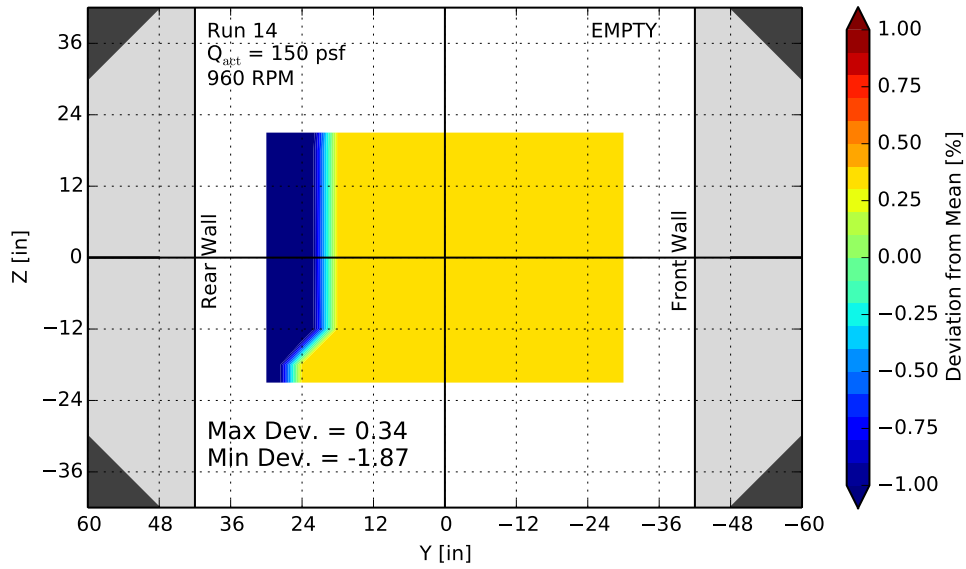
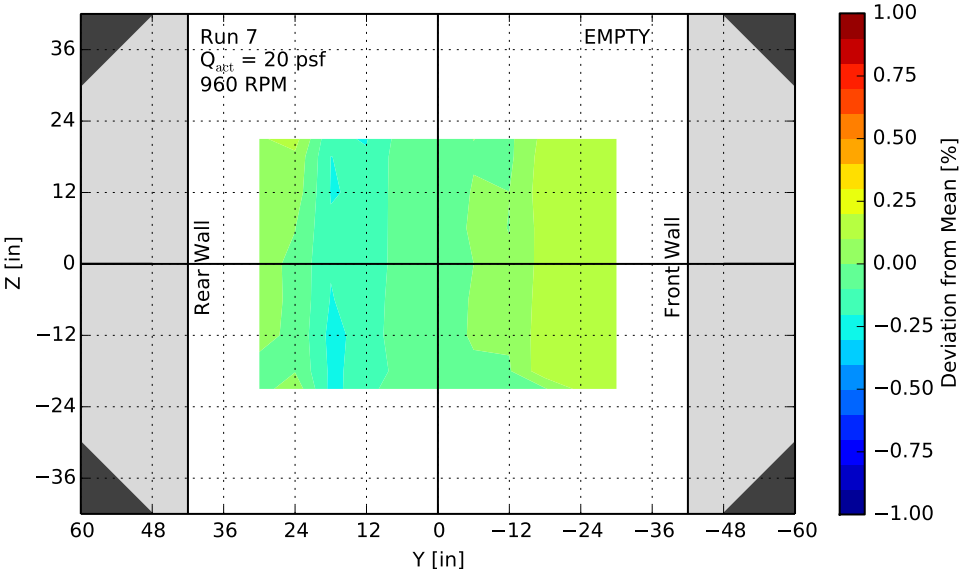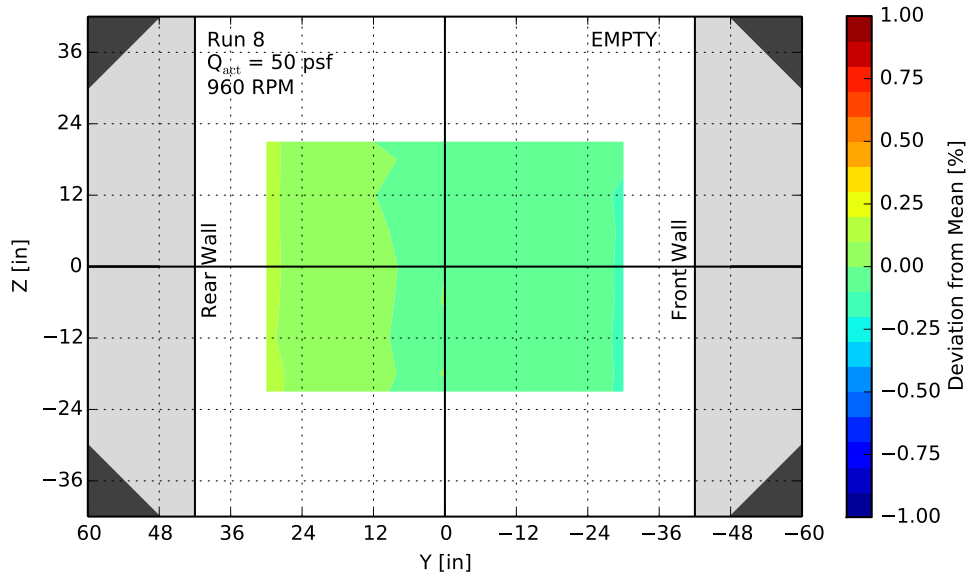Figure 5.14: Dynamic Pressure Variation at q_{act} of 150 psf, 960 RPM, 7x7ft Test Section
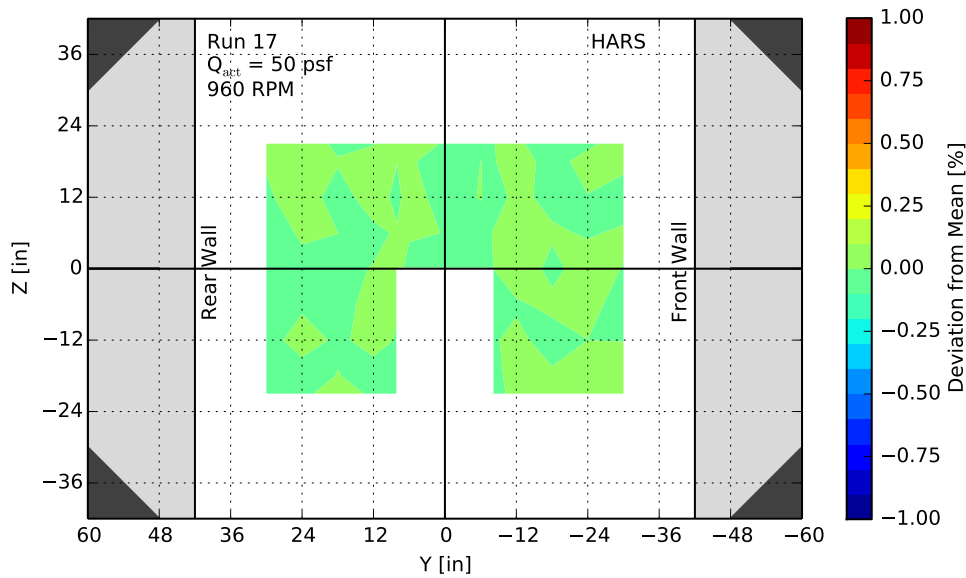
Figure 5.15: Dynamic Pressure Variation at q_{act} of 50 psf, 960 RPM, 7x7ft Test Section with HARS
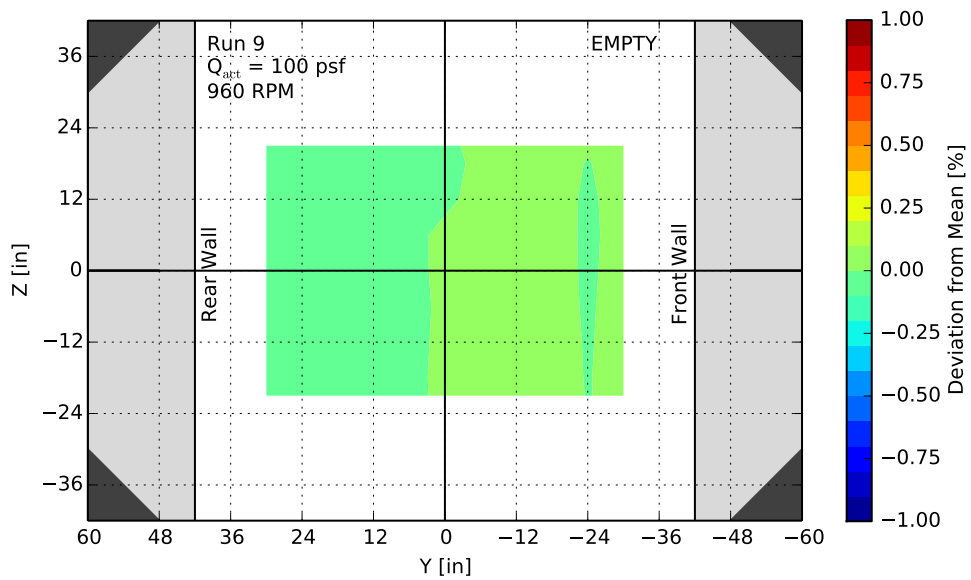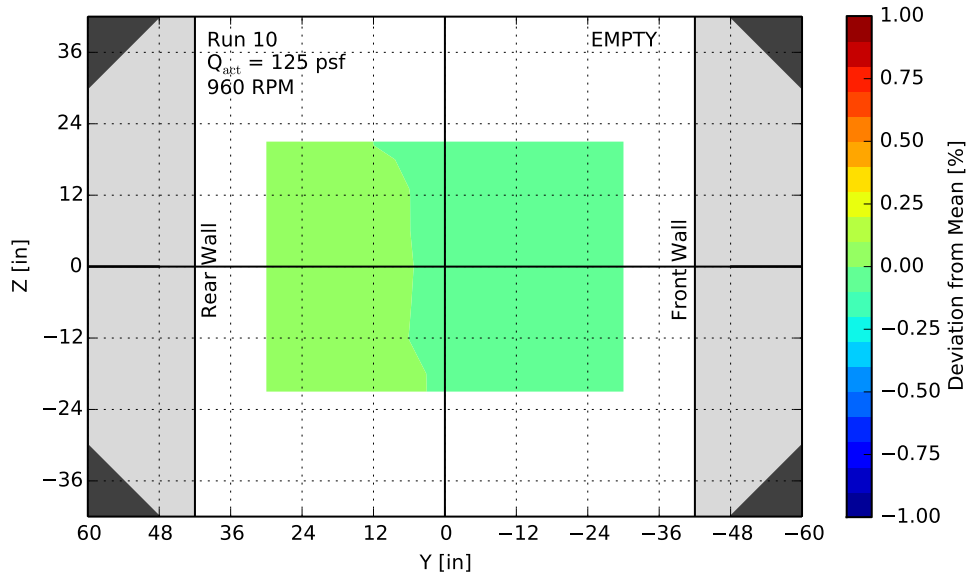
45
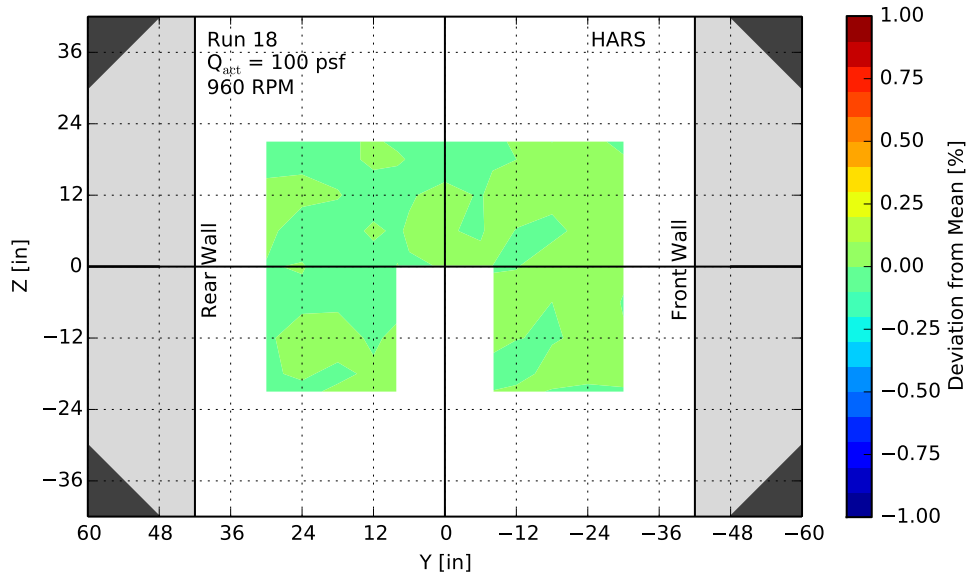
Figure 5.16: Dynamic Pressure Variation at q_{act} of 100 psf, 960 RPM, 7x7ft Test Section with HARS
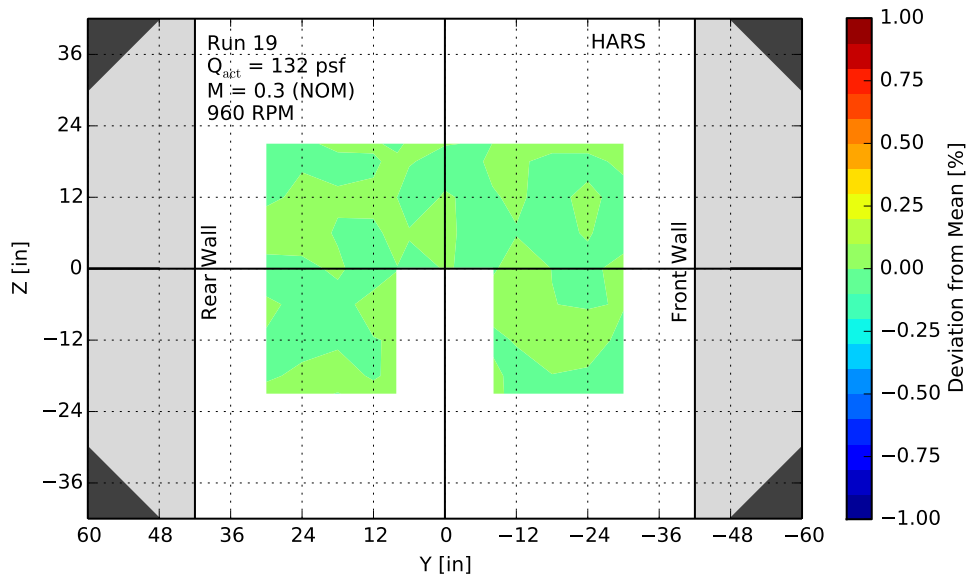
Figure 5.17: Dynamic Pressure Variation at q_{act} of 132 psf, 960 RPM, 7x7ft Test Section with HARS
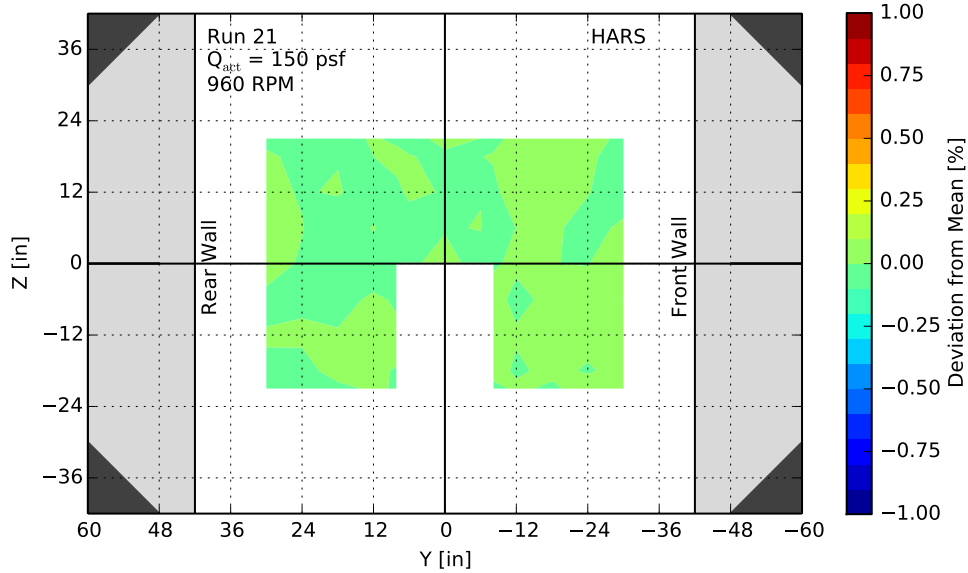
Figure 5.18: Dynamic Pressure Variation at q_{act} of 150 psf, 960 RPM, 7x7ft Test Section with HARS

The flow uniformity seen in both the 7 x 10 ft test, and the 7 x 7 ft test is adequate to claim uniform flow throughout the test section. Apart from two isolated incidences the flow uniformity for the reduced test section showed less than 1% deviation from the mean at any point, with the majority of cases being below 0.5%.

5.3 Splitter Plate Performance

The implementation of a splitter plate in the diffuser design was necessary to maintain the equivalent expansion angle below the recommended 3.5°. This addition was expected to increase the power required to drive at high speeds due to skin friction drag. Section 3.2 estimated the required additional power at Mach 0.4 ($q = 240$ psf) to be 196 HP. This was completed using an estimated skin friction coefficient of $C_{\text{F}} = 0.005$.

During testing, a high speed run was conducted before the splitter was installed. Maximum speed was not achieved due to day-time power constraints but the data is sufficient for comparing power requirements. A comparison of the non-splitter-plate vs splitter-plate-installed run can be seen in Figure 5.19. The incremental power required by the splitter plate is very low. Instead of C_{F}=0.005, a better estimate is C_{F}=0.0015. It is apparent that for the 7 x 7 ft test section, blade stall has occurred before expected. This will be discussed in a following section. However, it is clear that the preliminary assumption of α_{geo} being equal for the 7 x 10 ft and reduced test section cases lead to an inaccurate calculation of stall speed.
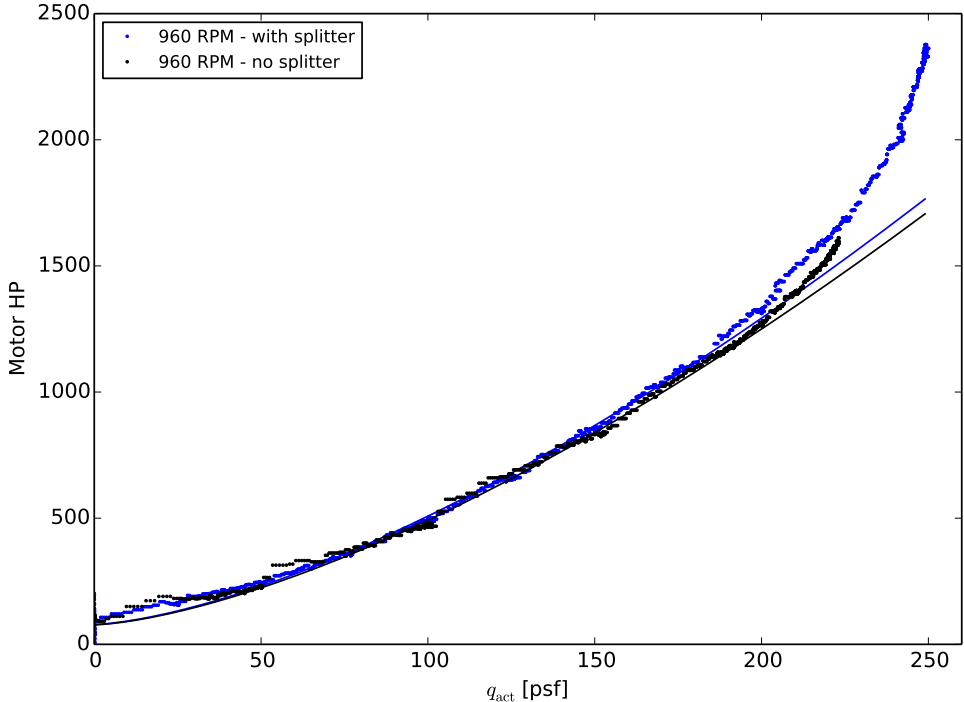
Figure 5.19: Comparison of pre-splitter plate and post-splitter plate installation

5.4 Diffuser Efficiency

The power curve slope is notably different between the 7 x 7 ft and 7 x 10 ft test sections. Because all other tunnel components are unchanging, this change in slope can be attributed to an improvement in efficiency of the new diffuser relative to the existing concrete diffuser. Guthery[1] (citing Barlow et al.[6]) outlined a procedure for determining the aerodynamic efficiency of a given wind tunnel section. Using Equation 3.2 an estimate of the change in efficiency from one run to another can be determined. Figure 5.20 shows a clear change in slope of the power curve between the 7 x 7 ft test section and the 7 x 10 ft test section, from $K = 0.011$ to $K = 0.00875$, an improvement of 20%.
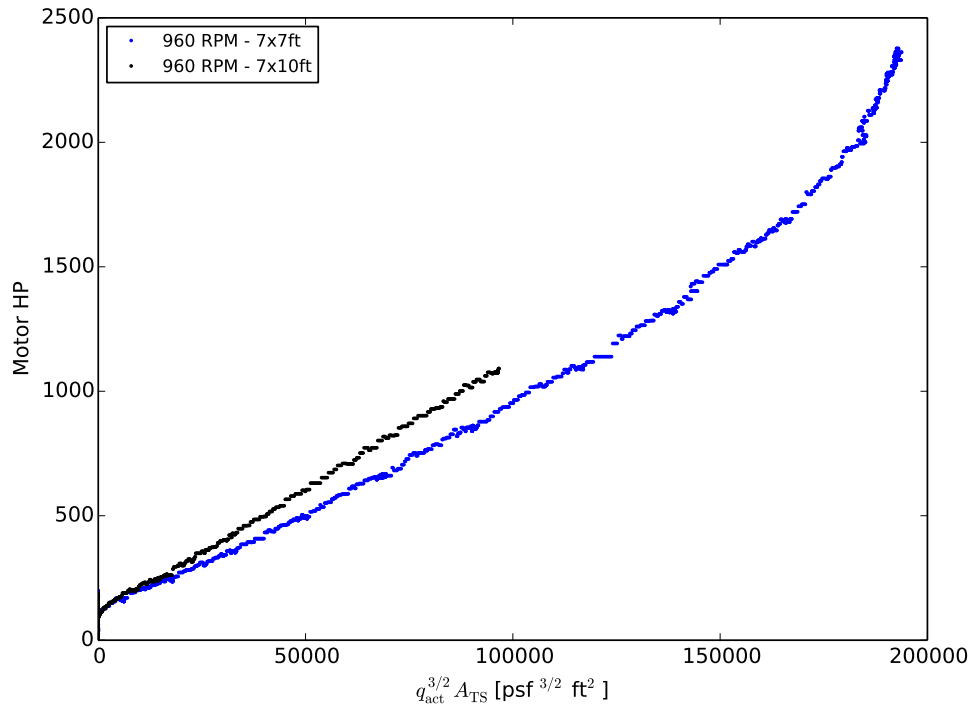
Figure 5.20: Change in aerodynamic efficiency between 7x7 ft and 7x10 ft test section

This unexpectedly better efficiency can be credited with causing a series of deviations from the initial predictions outline in Section 3. The following sections attempt to reconcile these differences and make future predictions for unknown tests conditions.

5.5 Blade Angle of Attack

Due to the change in aerodynamic efficiency of the newly designed diffuser, the preliminary assumption that blade stall can be predicted by only the advance ratio of $V_{\text{fan}}/R\omega$ is incorrect. In an attempt to predict future tests, a model for power required solely as a function of conditions at the power station is needed. This model can be used, as shown in Section 5.6, to determine the motor RPM setting for a given desired dynamic pressure. It is important to avoid post-stall regimes during testing to reduce power draw and flow non-uniformity.

$$P = V_{\text{fan}}A_{\text{fan}}\Delta p_{\text{fan}} + T\omega \tag{5.2}$$

Equation 5.2 represents the power required as a function of the change in pressure across the fan blades and the torque required to spin the fan. A crude aerodynamic approximation for fan performance can be used to expand Equation 5.2 into

$$P = R\omega A_{\text{fan}}q_{\text{fan}}\left[\underbrace{\frac{dC_{\text{L}}}{d\alpha}\frac{V_{\text{fan}}}{R\omega}\alpha}_{V_{\text{fan}}A_{\text{fan}}\Delta p_{\text{fan}}} + \underbrace{\frac{d^2C_{\text{D}}}{d\alpha^2}\alpha^2 + C_{\text{D},0}}_{T\omega}\right] \tag{5.3}$$

Where,

$$q_{\text{fan}} = \frac{1}{2}\rho V_{fan,rel}^2$$
$$= \frac{1}{2}\rho\left[(R\omega)^2 + (V_{\text{fan}})^2\right]$$

50

And,

$$V_{\text{fan}} = \sqrt{\frac{2q_{\text{TS}}}{\rho}} \frac{A_{\text{TS}}}{A_{\text{fan}}}$$

An expression for α as a function of the three aerodynamic constants, $\frac{dC_{\text{L}}}{d\alpha}$, $\frac{d^2C_{\text{D}}}{d\alpha^2}$, $C_{\text{D},0}$, and tunnel conditions can be found, using Equation 5.3 and Equation 3.2 . This expression can be seen in Equation 5.4. $C_{\text{D},0}$ can be found by Equation 5.5, where the other two constants are determined by adjustment until the raw data shows an $\alpha_{\text{stall}} = 15°$. This data can be seen in Figure 5.21

$$\frac{d^2C_{\text{D}}}{d\alpha^2}\alpha^2 + \frac{dC_{\text{L}}}{d\alpha}\frac{V_{\text{fan}}}{R\omega}\alpha - \frac{Kq_{\text{TS}}^{3/2}A_{\text{TS}}}{R\omega A_{\text{fan}}q_{\text{fan}}} = 0 \tag{5.4}$$

$$C_{\text{D},0} = \frac{P_0}{R\omega A_{\text{fan}}q_{\text{fan}}} \tag{5.5}$$
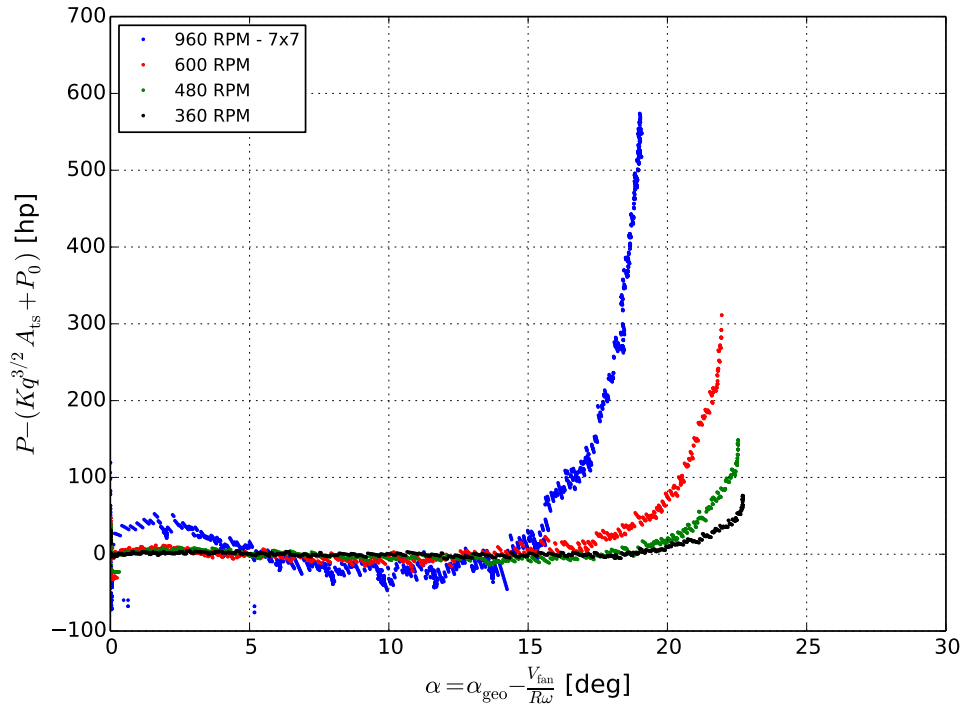
Figure 5.21: α vs Power offset from prediction

The true angle of attack is unknown and arbitrary for modeling purposes. For consistency with "typical" values, an arbitrary stall angle of $\alpha_{\text{stall}} = 15°$ was chosen for modeling purposes. In actuality, because of the large twist in a propeller blade, and a lack of ability to measure what the geometric angle of attack α_{geo} is at any given velocity, it is impossible to know the true angle of attack of the blades. However, by using a consistent model for the power required as given in Equation 5.3, prediction for the pre-stall regime of testing can be accomplished.

5.6 Testing Envelope

Ultimately, the LSWT requires a testing envelope in which test section dynamic pressures can be achieved within known limits on RPM and motor HP. By combining the results from Sections 5.1 to 5.5, a prediction of velocity in the pre-stalled regime of testing can be determined. However, limiting factors reduce the testing envelope below the 2400 HP maximum power draw as previously mentioned.

When testing at a higher dynamic pressure, various components of the wind tunnel begin to experience higher stresses. Of particular concern is the two turbulence screens located just before the contraction. These screens were designed only for 100 psf operation in the 7 10 ft test section and their ability to withstand substantially higher loads is unknown. Due to this need, a limit on the pressure drop across the screens is implemented for safety. The change in pressure across a given tunnel component, ΔP, can be found by

$$\Delta P = K_l q_l \tag{5.6}$$

where the subscript l denotes local conditions, and K_l is the local efficiency. This local efficiency can be combined into the overall efficiency of the tunnel, K by

$$K = \sum_l K_l \tag{5.7}$$

from Barlow et al.[6]. For the LSWT, Guthery [1] determined that $K_l = 0.57$ for each of the two screens.

In practice, the tunnel is controlled based on q_{act} in the test section. Additionally, the K_l of the screens can change with time based on the amount of dirt and debris lodged within the screens. It is for this reason that two separate mechanisms are put in place to avoid a failure of the screens. The first limiter is the addition of a real-time readout of the pressure drop across the screens, which is to always be maintained below a specified maximum. The second limiter is a limit of q_{act} in the test section. This second limiter takes into account the pressure drop across the screen, the maximum horsepower available, and the stall speed of the fan.

The maximum rated pressure drop across the screens, ΔP_{m}, was determined based on historical data as the equivalent pressure drop at a q_{act} of 130 psf in the 7 x 10 ft test section. This corresponds to a q_{act} of 250 psf in the 7 x 7 ft test section. Additionally, there is a contingency rating of the equivalent pressure drop, ΔP_{c}, at q_{act} of 145 psf for the 7 x 10 ft case, and 280 psf for the reduced test section. This contingency can be reached safely, but must only be maintained for up to one minute of operation, with a physical examination of the screens after each run at this contingency level.

In order to determine the limits on q_{act}, Equation 5.4 was solved for q_{act} with α ranging from 0° to 15°, $\frac{dC_{\text{L}}}{d\alpha} = 0.25$, and $\frac{d^2 C_{\text{D}}}{d\alpha^2} = 0.005$. This resulting q_{act} was then substituted into Equation 3.2 to find the power draw for that test condition.

Figure 5.22 shows the results for the 7 x 7 ft test section, with Figure 5.23 showing the 7 x 10 ft case. Both the daytime and nighttime horsepower limits of 1600 HP and 2400 HP, respectively, are shown. Additionally, the ΔP_m and ΔP_c limits are indicated.
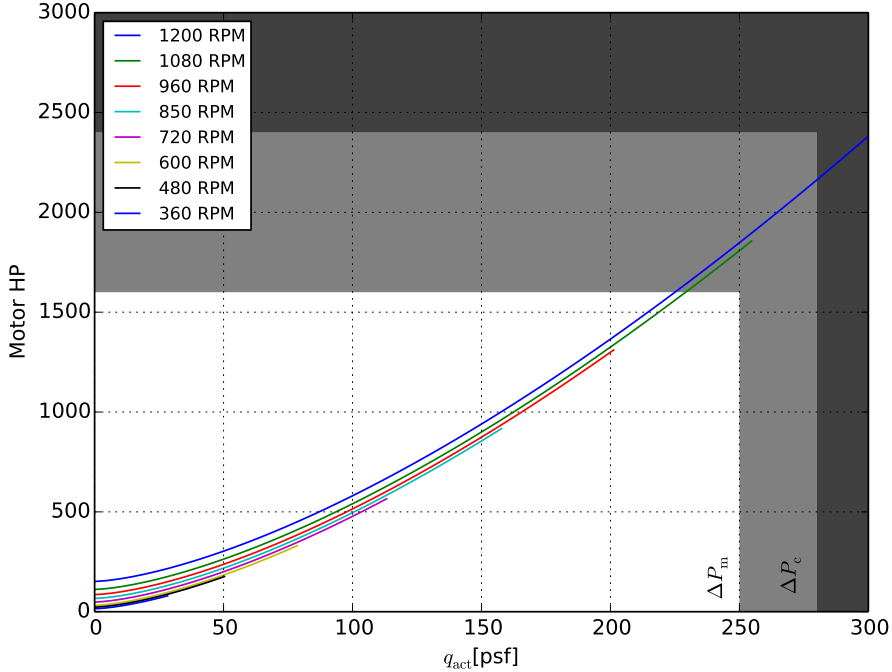
Figure 5.22: 7x7 ft test section power vs q_act predictions
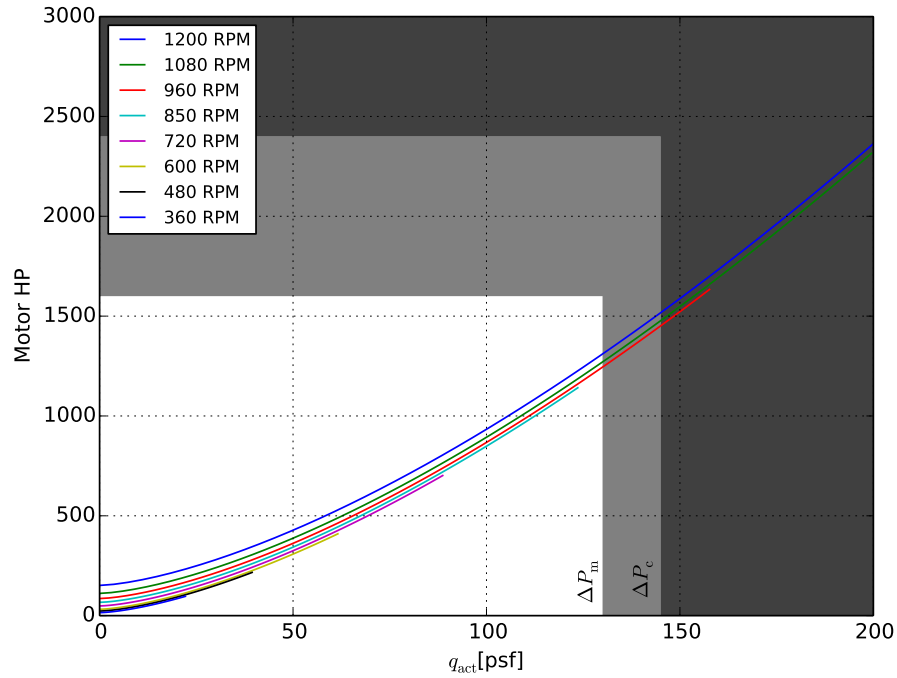
Figure 5.23: 7x10 ft test section power vs q_{act} predictions

Tables 5.1 and 5.2 show a breakdown of the results from Figures 5.22 and 5.23. Each motor RPM reading has both a maximum and contingency q_{act} associated with it. For the cases in which power required or blade stall is the initial limiting factor, no contingency is given.

	RPM	Maximum			Contingency		
		q_{act}[psf]	Vel [mph]	Motor HP	q_{act}[psf]	Vel [mph]	Motor HP
7x7ft Test Section	1200	250	313	1848	280	331	2162
	1080	250	313	1808	255	316	1856
	960	201	280	1311	-	-	-
	850	158	249	917	-	-	-
	720	113	210	565	-	-	-
	600	79	176	331	-	-	-
	480	50	140	176	-	-	-
	360	28	105	80	-	-	-
7x10ft Test Section	1200	130	225	1310	145	238	1517
	1080	130	225	1270	145	238	1477
	960	130	225	1245	145	238	1451
	850	124	220	1141	-	-	-
	720	89	187	702	-	-	-
	600	62	156	410	-	-	-
	480	39	124	216	-	-	-
	360	22	93	97	-	-	-

Table 5.1: Night power limited maximum and contingency dynamic pressure limits

	RPM	Maximum			Contingency		
		q_{act}[psf]	Vel [mph]	Motor HP	q_{act}[psf]	Vel [mph]	Motor HP
7x7ft Test Section	1200	225	297	1600	-	-	-
	1080	229	299	1600	-	-	-
	960	201	280	1311	-	-	-
	850	158	249	917	-	-	-
	720	113	210	565	-	-	-
	600	79	176	331	-	-	-
	480	50	140	176	-	-	-
	360	28	105	80	-	-	-
7x10ft Test Section	1200	130	225	1310	145	238	1517
	1080	130	225	1270	145	238	1477
	960	130	225	1245	145	238	1451
	850	124	220	1141	-	-	-
	720	89	187	702	-	-	-
	600	62	156	410	-	-	-
	480	39	124	216	-	-	-
	360	22	93	97	-	-	-

Table 5.2: Day power limited maximum and contingency dynamic pressure limits

Note that for many of the cases in which no contingency is given, the limiting factor was blade stall. For these cases, particularly in the 7 x 7 ft test section, the ability remains to achieve higher test section dynamic pressures. Until a model detailing post-stall characteristics of the LSWT blades exists, predictions to these higher dynamic pressures remain unknown.

6. CONCLUSIONS AND RECOMMENDATIONS

The goals of this study were to achieve a maximum working velocity in the LSWT of Mach 0.4 while maintaining acceptable flow uniformity. By reinforcing existing tunnel structure, upgrading and installing a reduced test section, and manufacturing a more efficient, easy-to-install diffuser these goals were met. The newly designed reduced test section has a cross section of 7 x 7 ft with a diffuser of just over 25 feet in length. This diffuser uses steel wall panels supported by steel structure attached to permanent mounting points within the existing concrete diffuser. In addition to the steel diffuser, a wooden splitter plate was installed as well yielding an effective expansion angle of $\theta_{eq} = 2.45°$. This expansion angle is well below the recommended maximum diffuser angle of $\theta_{eq} = 3.5°$. By extending the length of the diffuser and reducing the effective expansion, an increase in efficiency was achieved. Overall a measure of aerodynamic losses, K, changed from $K = 0.011$ for the 7 x 10 ft test section to $K = 0.00875$ for the reduced test section, a 20% increase in efficiency.

It was also clear after installation of the newly designed diffuser that conforming to the design rules outlined in Section 4.2 allowed for straight-forward installation. However, future designs should attempt to allow for more accurate and repeatable adjustments to fit within unknown geometries. While the amount of match drilling was not more than expected, the inability to fix adjustment points during installation made follow up installations difficult as those adjustments had to be made again.

During testing to the maximum power available of 2400 HP, a maximum speed of Mach 0.408 ($q_\text{act} = 250$psf) was achieved while maintaining flow uniformity throughout the test section. On average, the deviation from average dynamic pressure for any case in the reduced test section was less than 1% while many cases maintained less than 0.5% deviation.

Additionally, a new model for power performance in the pre-blade-stall regime of testing was developed yielding the ability to predict the test conditions of future models. In the future, it may be necessary to expand to this model to account for behavior beyond stall onset for the reduced test section. Blade stall exhibits a slow onset for the reduced section so operation is feasible in this regime.

By implementing the new model for power performance we can see that a maximum dynamic pressure of 280 psf is attainable. This is only limited by the self-imposed contingency limit to protect the turbulence screens. In future tests, a more robust screen design may allow for even higher speeds to be achieved in the reduced test section.

REFERENCES

[1] Guthery, J. M., *Assessment of Flow Efficiency Through a Closed Circuit Wind Tunnel with Recommendations for Improvements*, Master's thesis, Texas A&M University, 2013.

[2] Unkown, "Subsonic Wind Tunnel - 4," Cushing Memorial Library and Archives, Texas A&M University, College Station, Texas, 1958.

[3] Unkown, "Wind Tunnel Building - 8," Cushing Memorial Library and Archives, Texas A&M University, College Station, Texas, 1946.

[4] Sahoo, D., *Experimental Analysis of the Vorticity and Turbulent Flow Dynamics of a Pitching Airfoid at Realistic Flight (Helicoper) Conditions*, Ph.D. thesis, Texas A&M University, 2008.

[5] Hidore, J. P., *Investigation of Data Quality For Wind Tunnel Internal Balance Testing*, Master's thesis, Texas A&M University, 2013.

[6] Barlow, J. B., Rae Jr., W. H., and Pope, A., *Low-Speed Wind Tunnel Testing*, Wiley & Sons, Unites States of America, 1999.

[7] Bradshaw, P. and Pankhurst, R. C., "The Design of Low-Speed Wind Tunnels," 1964.